Nano Research
2022, 15(1): 123–144
ISSN 1998-0124 CN 11-5974/O4
https://doi.org/10.1007/s12274-021-3500-2

Review Article

p-/n-Type modulation of 2D transition metal dichalcogenides for electronic and optoelectronic devices

Songyu Li[1], Yang Ma[2], Nabonswende Aida Nadege Ouedraogo[2], Famin Liu[1] (✉), Congya You[2], Wenjie Deng[2], and Yongzhe Zhang[2] (✉)

[1] *School of Physics, Beihang University, Beijing 100191, China*
[2] *Key Laboratory of Advanced Functional Materials, Ministry of Education, College of Materials Science and Engineering, Beijing University of Technology, Beijing 100124, China*

Received: 20 December 2020 / **Revised:** 1 April 2021 / **Accepted:** 6 April 2021

ABSTRACT

Two-dimensional layered transition metal dichalcogenides (TMDCs) have demonstrated a huge potential in the broad fields of optoelectronic devices, logic electronics, electronic integration, as well as neural networks. To take full advantage of TMDC characteristics and efficiently design the device structures, one of the most key processes is to control their p-/n-type modulation. In this review, we summarize the p-/n-type modulation of TMDCs based on diverse strategies consisting of intrinsic defect tailoring, substitutional doping, surface charge transfer, chemical intercalation, electrostatic modulation, and dielectric interface engineering. The modulation mechanisms and comparisons of these strategies are analyzed together with a discussion of their corresponding device applications in electronics and optoelectronics. Finally, challenges and outlooks for p-/n-type modulation of TMDCs are presented to provide references for future studies.

KEYWORDS

transition metal dichalcogenides, p-/n-type modulation, doping method, electronic devices, optoelectronic devices

1 Introduction

Nowadays, the scaling reduction of silicon-based integrated circuits (IC) has hit a bottleneck due to their physical limitation of quantum confinement effect [1–3]. To ensure the evolution of the post-Moore era, it is urgent to explore new semiconductor processing routes and upgraded hardware architectures [4–10]. Among various novel materials, the two-dimensional (2D) materials are promising candidate to overcome the scaling limitation in regard to their characteristic of atomically thin thickness [11, 12]. One kind of them, namely transition metal dichalcogenides (TMDCs) are widely studied in the area of electronic and optoelectronic devices due to their attractive characteristics such as the absence of dangling bonds [13–15], tunable band gap [16, 17], large-scale fabrication capability [18–23], and compatibility to silicon complementary metal-oxide-semiconductor (CMOS) [24–26]. Moreover, TMDCs display a huge application prospect in the ultrafast neural network machine vision with a throughput of 20 million bins per second due to a parallel design of image sensing and data processing [27, 28]. Besides, their unique interlayer excitons as well as light-matter interactions have given TMDCs a vast potential to break through the traditional working mechanism of optoelectronics [29–31].

To achieve practical applications of TMDCs in the semiconductor devices, it is quite necessary to design metal-semiconductor contacts and semiconductor junctions which constitute the fundamental elements for the fabrication of almost all the semiconductor devices such as p-n junction, bipolar junction transistor (BJT), field-effect transistor (FET), etc. [32, 33]. Moreover, the structures and performances of these devices are principally depending on the locally p- or n-type modulation to optimize their Schottky barriers, contact resistances, and depletion regions [34, 35]. The traditional p-/n-type modulation techniques for bulk materials (Si, GaAs, etc.) include thermal diffusion and ion implantation, of which modulation principle is doping in the substitutional and interstitial ways [36]. However, the p-/n-type modulation of TMDCs is quite different from that of bulk materials. Their unique characteristic of ultrahigh specific surface area makes them extremely sensitive to crystal defects [37–39], impurities [40–43], contacts [15, 44–49], and interfaces [43, 50–52], which would largely interfere with the real p/n-type levels and bring a huge challenge to the applications of TMDC-based devices. Nevertheless, their atomically thin thickness also presents some new possible approaches in modulating their p-/n-type levels by controlling the sensitive factors aforementioned [53–56]. These new modulation strategies therefore contribute to more flexible design and applications of TMDC-based semiconductor devices [34, 57–59].

Since research on the p-/n-type modulation of TMDCs has been widely developed through these past years, it is necessary to summarize the related techniques and discussions as references for future studies. Herein, we focus on the recent progress of TMDC-based p-/n-type modulation and their advanced applications in electronic and optoelectronic devices. Six modulation strategies including intrinsic defect tailoring, substitutional doping, surface charge transfer, chemical

Address correspondence to Famin Liu, fmliu@buaa.edu.cn; Yongzhe Zhang, yzzhang@bjut.edu.cn

intercalation, electrostatic modulation, and dielectric interface engineering are described, along with the analyses in detail of their advantages and disadvantages. At last, based on the current progress, a conclusion about the remaining challenges and outlooks for the p-/n-type modulation of TMDCs will be made in this promising field.

2 p-/n-Type modulation strategies

The inherent variation of p-/n-type modulation is the shift of Fermi-level. When applying p-type modulation, the Fermi-level would approach the valence band, while n-type modulation would lead the Fermi-level close to the conduction band. The energy band engineering could be achieved by following six modulation strategies according to the differences in modulation process: intrinsic defect tailoring, substitutional doping, surface charge transfer, chemical intercalation, electrostatic modulation, and dielectric interface engineering. Each of them involves multiple implementation methods as shown in Fig. 1. The following paragraphs will analyze the recent progress and modulation mechanisms of these strategies, aiming to provide references and insight for future studies on the p-/n-type modulation and device applications of TMDCs.

2.1 Intrinsic defect tailoring

It is well known that the intrinsic lattice structure of a material is not perfect. Indeed, different kinds of crystal defects are unavoidably or intentionally generated, such as vacancies, interstitials, and antisites, that would severely disturb the periodic potential field of the host lattice, generate defect energy levels and even provoke phase transitions [60–62]. Some defects with relatively shallow energy levels would lead to the change of carrier distribution and eventually regulate conduction properties [63–65]. Thus, TMDCs could be intrinsically doped by the controllable intrinsic defect engineering, which has the advantages of easy patterning without any implanting impurity [66–68]. When synthesizing TMDCs, the defect tailoring and doping effect level could be *in-situ* modulated by stoichiometric ratio [67, 69]. As shown in Figs. 2(a) and 2(b), the p-type (high Se/Pt ratio) and n-type (low Se/Pt ratio) doping of $PtSe_2$ were achieved during the *in-situ* chemical vapor deposition (CVD) growth. The high Se/Pt ratio was realized by a slow cool down process with a continuous supply of Se precursor, while the low Se/Pt ratio was achieved by a rapid cool down process followed by Se precursor removal. Besides the *in-situ* growth presented above, the defects could be also created by post-growth approaches, that all have the advantage of patterned doping capability, for instance, chemical treatment [66], plasma or electron beam etching [68, 70, 71], and light illumination [72]. A great example of chemical treatment for the intrinsic defect tailoring of MoS_2 is presented in Fig. 2(c) [66]. Due to the introduction of electrons by HO_2^- that led to the breakage of S–Mo bonds, some patterned S vacancies were generated on MoS_2. The uniform reduction of S composition could be depicted by the Auger electron spectroscopy (AES) mapping of S element (Fig. 2(d)). As for the light-induced defect tailoring, Te interstitial defects were generated in $MoTe_2$ after ultraviolet (UV) light illumination (Fig. 2(e)) that transformed the conduction type of $MoTe_2$ from n^--type to n^+-type (Fig. 2(f)) [72]. On the contrary, the doping level could be modulated by the defect healing process [72–74]. The most common intrinsic defects of TMDCs are chalcogen vacancies (more than 10^{13} cm^{-2} for mechanical exfoliation and CVD MoS_2) owing to their low formation energy [54, 64, 65, 75]. Figure 2(g) depicts the S vacancy self-healing process achieved by sulfur adatom clusters on MoS_2 surface through a poly(4-styrenesulfonate)-induced hydrogenation process. After the healing process, n-type doping effect of S vacancies was

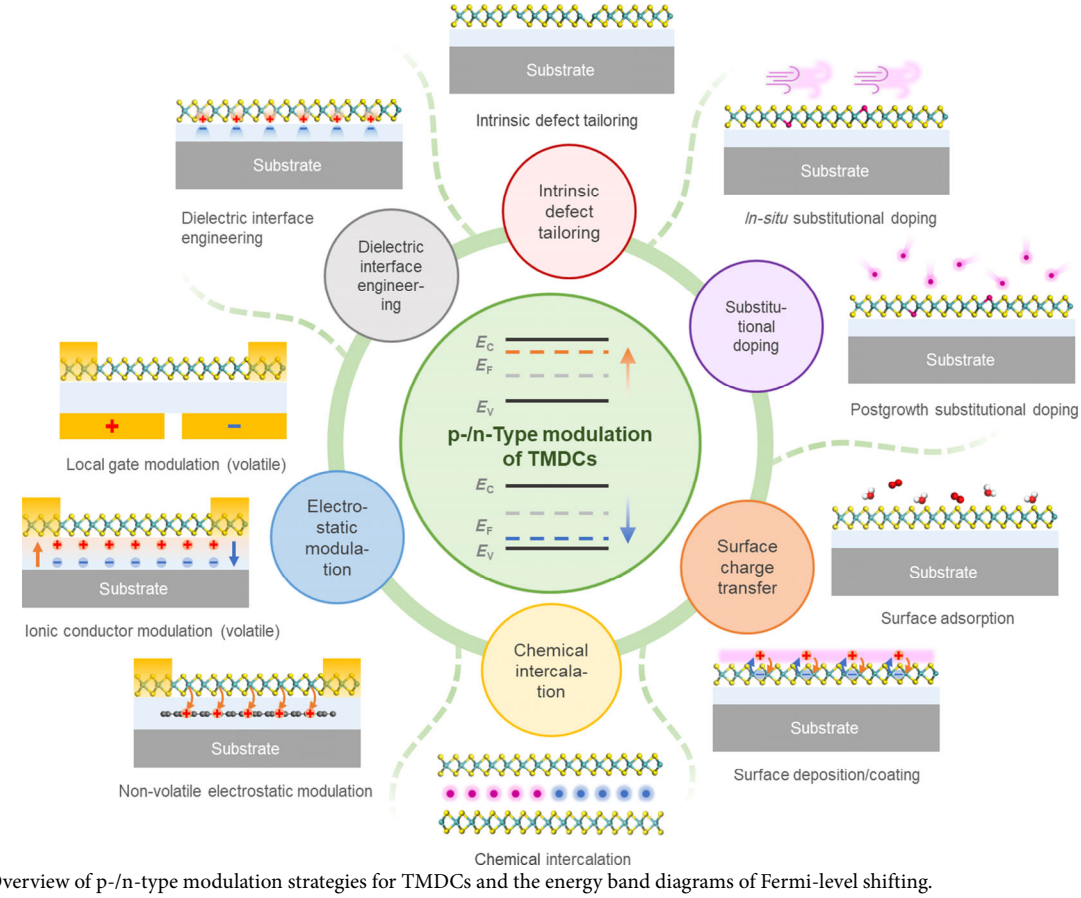

Figure 1 Overview of p-/n-type modulation strategies for TMDCs and the energy band diagrams of Fermi-level shifting.

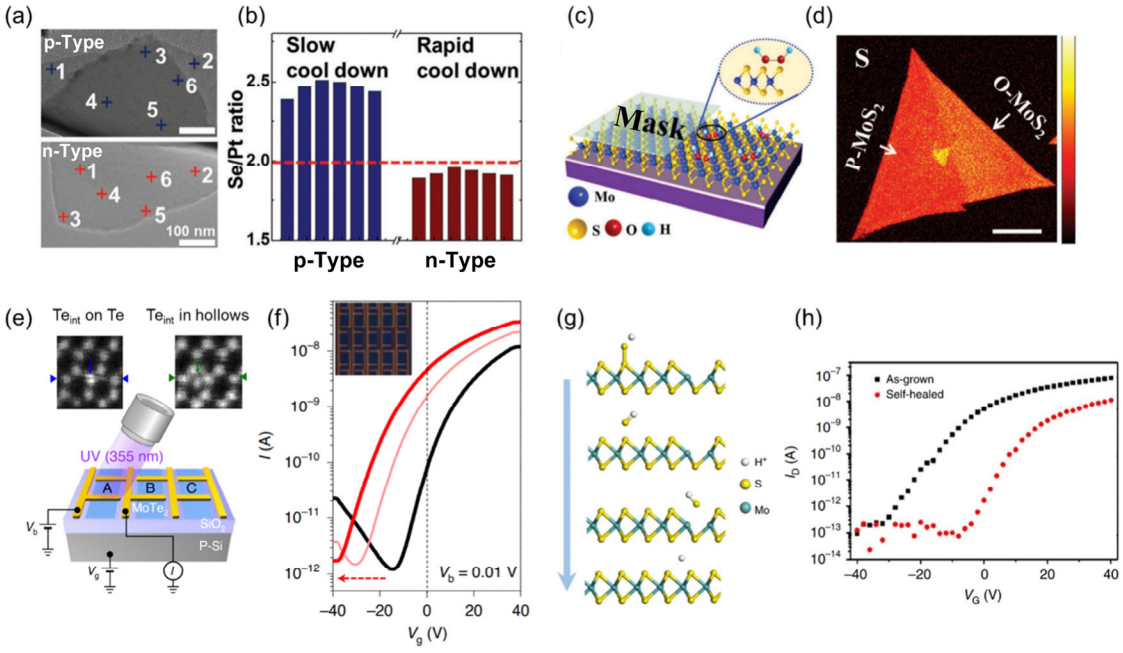

Figure 2 Doping methods based on intrinsic defect tailoring. (a) and (b) Low-magnified transmission electron microscopy (TEM) images and elemental ratios of two conduction types of $PtSe_2$ controlled by selenization process. Reproduced with permission from Ref. [67], © WILEY-VCH Verlag GmbH & Co. KGaA 2018. (c) Schematic diagram of defect modulation of MoS_2 by H_2O_2 solution process. (d) Auger electron spectroscopy element mapping of S before and after defect modulation. Reproduced with permission [66], © WILEY-VCH Verlag GmbH & Co. KGaA 2019. (e) Schematic diagram of n-type modulation of 2H-$MoTe_2$ written by UV illumination and the corresponding scaning transmission electron microscope (STEM) images of Te interstitial defects. (f) Transfer curves of 2H-$MoTe_2$ FET with different n-type levels. Reproduced with permission [72]. © The Author(s), under exclusive licence to Springer Nature Limited 2020. (g) Chemical structure change showing the poly(4-styrenesulfonate)-induced S vacancy self-healing (SVSH) of monolayer MoS_2. (h) Transfer curves of a monolayer MoS_2 transistor before and after SVSH indicating the remission of S vacancy-induced n-type doping. Reproduced with permission [74], © The Author(s) 2017.

alleviated (Fig. 2(h)). Even some defect-related doping results have been demonstrated experimentally according to the aforementioned studies, some defect energy level variations (such as S vacancy defects) have not reached a consensus, and their inherent mechanisms are not that explicit yet [38, 69, 76–78]. These aforementioned limitations might originate from additional damages (other vacancies, chemical clusters, local curling, and deformations) caused by ion/electron etching, light illumination, etc., that are not comprehensively analyzed.

2.2 Substitutional doping

The substitutional doping is one of the most important strategies for the p-/n-type modulation of traditional bulk materials. With this strategy, atoms in the original material are replaced by some impurities. To ensure the achievement of substitutional doping, the formation energies of dopants with the host lattice should be relatively low. For example, the promising substitutional dopants of Group VIB TMDC monolayers should usually be lower than 1 eV [79]. The main function of these dopants is to provide extra electrons or holes by taking use of their different electron distribution from that of the original components. As a result, the dopants with shallow impurity energy levels in the energy bandgap of host lattice should be chosen. However, the ionization energies of promising dopants in TMDCs are naturally one order of magnitude higher than that of bulk materials (530 meV for Nb dopants in monolayer MoS_2), due to the weak response of dopant states to quantum confinement [56]. Thus, TMDCs desire relative high doping concentrations, which is generally percentage level to ensure the change in conductivity [80, 81]. According to the structure of TMDCs (MX_2, M = transition metals, such as Mo, W; X = S, Se, and Te), substitutional doping could occur at both M and X sites [17, 82]. Some elements adjacent to M and X are the potential candidates for MX_2 doping [56]. Depending on the implementations process, substitutional doping could be divided into *in-situ* substitutional doping and postgrowth substitutional doping. Different substitutional doping methods together with their effective dopants are listed in Table 1 as below.

Table 1 A summary of typical dopants and their properties for the substitutional doping of TMDCs

Dopant	Doping type	Method	Material	Concentration (cm^{-2})	References
Nb	p-Type	CVT synthesis	MoS_2	1.8×10^{14}	[83]
Nb	p-Type	CVD synthesis	MoS_2, WS_2	10^{13}–10^{14}	[84–91]
V	p-Type	CVD synthesis	MoS_2, WS_2	—	[92, 93]
O	p-Type	Plasma treatment	MoS_2	—	[94, 95]
O	p-Type	Photon assistance	MoS_2	—	[72, 76]
O	p-Type	Thermal diffusion	$MoTe_2$	5×10^{12}	[96]
CH-group	p-Type	Plasma treatment	MoS_2, WS_2	—	[95, 97, 98]
N	p-Type	CVD synthesis	WS_2	—	[99]
N	p-Type	Plasma treatment	WS_2	3.8×10^{11}	[100, 101]

(Continued)

Dopant	Doping type	Method	Material	Concentration (cm^{-2})	References
P	p-Type	Plasma treatment	MoS_2	2.4×10^{12}	[102, 103]
P	p-Type	Photon assistance	MoS_2	—	[104]
Sn	n-Type	Thermal diffusion	WS_2	—	[105]
Re	n-Type	CVD synthesis	MoS_2	2.1×10^{12}	[93, 106, 107]
Mn	n-Type	CVD synthesis	MoS_2	—	[108]
Fe	n-Type	CVD synthesis	MoS_2, WS_2	—	[91, 93]
Cl	n-Type	CVD synthesis	MoS_2	1.3×10^{12}	[109]

2.2.1 *In-situ substitutional doping*

In-situ substitutional doping is the doping process that occurs during the material growth, for which the dopants would be one of the precursors together with the original chemicals. This doping method could achieve a uniform doping result rather than locally patterned doping. Therefore, its main function in p-/n-type modulation is to regulate the background conductivity of the material. For the p-type *in-situ* substitutional doping of TMDCs, there are some examples in which Nb and V atoms were doped in Group VIB TMDCs, which turned out to be an practical p-type doping method [83–89, 92, 93]. Compared with Mo and W, Nb has less outer electrons so as to provide more density of states around the valence band maximum, thus contributing to p-type doping of MoS_2 or WS_2 [56, 88]. The initial experimental achievements of this doping process are Nb-doped MoS_2 samples which were obtained by chemical vapor transport (CVT) in sealed tube and by CVD sulfurization process [83, 84]. A p-n junction consisted of Nb-doped MoS_2 and undoped MoS_2 was fabricated to verify a clear rectification characteristic (Fig. 3(a)). It should be mentioned that the above Nb doping results are only realized on bulk MoS_2. For Nb-doped MoS_2 monolayers cases, the samples were synthesized by solid source chemical vapor deposition (CVD_{SS}) and metal-organic chemical vapor deposition (MOCVD), resulting in weak ambipolar (dopant percentage = 0.8%) and degenerate p-type (dopant percentage = 19%), respectively [85, 90]. A distinct p-type doping result was achieved on such a high doping percentage, that matches well with the high ionization energies of TMDCs [81]. Besides Nb-doped MoS_2, a Nb-doped WS_2 sample was acquired by CVD growth with liquid-phase precursor (Fig. 3(b)), which is further confirmed by high-angle annular dark field scanning transmission electron microscopy (HAADF-STEM) and transfer curve characterization (Figs. 3(c) and 3(d)) [89]. For the n-type doping of TMDCs, some other transition metals, such as Re, Mn, Fe, and Co, could be used, as their outer electrons are more than those of group VIB metals [93, 106–108, 110]. Besides the doping effects, some of these dopants could bring magnetism properties for spintronics as well, benefiting from the variations of the anti-bonding defect levels in the bandgaps [110–113].

The main group elements could also be the substitutional impurities for the element X (MX_2). As for p-type doping in this case, the elements of group IV and V (such as the elements of C, N, P, etc.) that have fewer outer electrons compared with element X, could provide extra holes for TMDCs. However, it is challengeable to realize an adequate p-type *in-situ* substitutional doping with them due to their generally strong

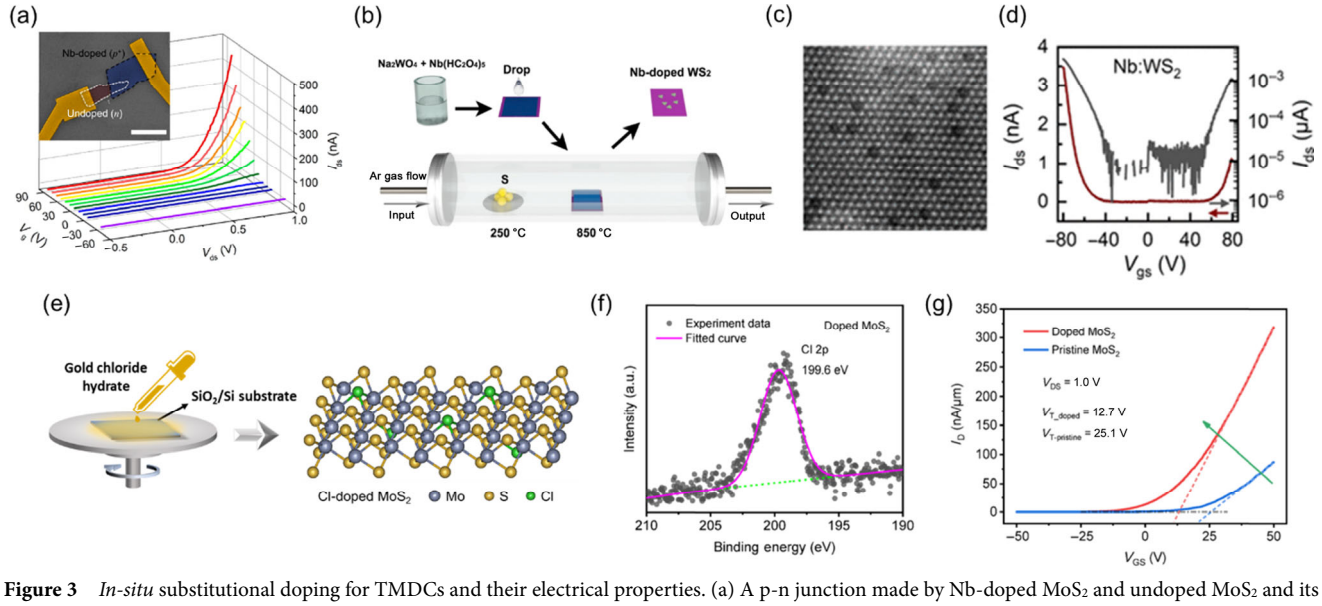

Figure 3 *In-situ* substitutional doping for TMDCs and their electrical properties. (a) A p-n junction made by Nb-doped MoS_2 and undoped MoS_2 and its electrical properties with different V_{DS} and V_{GS}. Reproduced with permission from Ref. [83], © American Chemical Society 2014. (b) Schematic diagram of the CVD synthesis for Nb-doped WS_2 by liquid-phase precursor. Reproduced with permission from Ref. [89], © American Chemical Society 2019. (c) HAADF-STEM image of Nb-doped WS_2 at the edge region. Reproduced with permission from Ref. [89], © American Chemical Society 2019. (d) Transfer curves on the linear and logarithmic scale of Nb-doped WS_2. Reproduced with permission from Ref. [89], © American Chemical Society 2019. (e) Schematic diagram of the CVD synthesis for Cl-doped MoS_2 with chemically pretreated substrate. Reproduced with permission from Ref. [109], © American Chemical Society 2019. (f) X-ray photoelectron spectroscopy (XPS) for the Cl-doped MoS_2 showing the presence of Cl in MoS_2. Reproduced with permission from Ref. [109], © American Chemical Society 2019. (g) Transfer curves of Cl-doped and pristine MoS_2 FETs. Reproduced with permission from Ref. [109], © American Chemical Society 2019.

chemical bonds (C and N) or various material forms (P). Despite the aforementioned difficulties, a N-doped WS_2 was successfully synthesized by a sulfurization process of WO_xN_y film yet [99]. As for n-type doping, the X site substitutions by group VII elements are promising alternatives [50, 56]. An *in-situ* n-type doping of MoS_2 by Cl was successfully achieved by CVD synthesis with a chemically pretreated substrate (Figs. 3(e) and 3(f)) [109]. The Cl-doped MoS_2 FET showed a more n-type conduction and a lower threshold voltage than the pristine samples (Fig. 3(g)).

2.2.2 *Postgrowth substitutional doping*

Patterned doping is one of the prerequisites for fabricating semiconductor devices and integrated circuit, however, it is hard to realize this goal through *in-situ* substitutional doping process. Compared with *in-situ* substitutional doping, postgrowth substitutional doping could achieve a more flexible patterned doping with a mask, which is a process of low-level reconstruction of crystal lattice by energetic dopants. However, TMDCs are more sensitive to crystal defect than bulk materials. Therefore, finding out a method to accurately control the vacancy creations and dopant occupations are the key to its application for TMDCs.

Postgrowth substitutional doping of TMDCs could be divided into three kinds of doping methods: low energy plasma treatment, thermal diffusion, and photon-assisted substitutional doping. Among them, plasma treatment is one of the most commonly used doping processes, which first implants the energetic dopant ions into the host lattice to create vacancies, and then some dopants with depleted energies fill in the vacancies to finish the substitutional doping process [80]. However, the plasma treatment energy used for bulk materials is so high that it is much easier to penetrate TMDCs as their ultrathin thickness (< 1 nm for monolayers) [114, 115]. Thus, it is necessary to lower the implant energy to a milder level during plasma treatment of TMDCs (≤ 10 keV for ion energy or ≤ 100 W for radio frequency (RF) power) [94, 97, 100, 101]. With this method, several plasma treatment processes using N, P, O, CH-groups are reported and the doping level could be well modulated by adjusting gas flow, plasma power and treatment time [94, 95, 97, 98, 100–103]. For example, WS_2 monolayers was controllably p-type doped by CH-group and the doping levels could be regulated by CH_4 flows (Fig. 4(a)) [97]. A clear S monovacancy and CH on S sites could be characterized by the atomic-resolution HAADF-STEM image as shown in Fig. 4(b) that represents the two doping steps of plasma

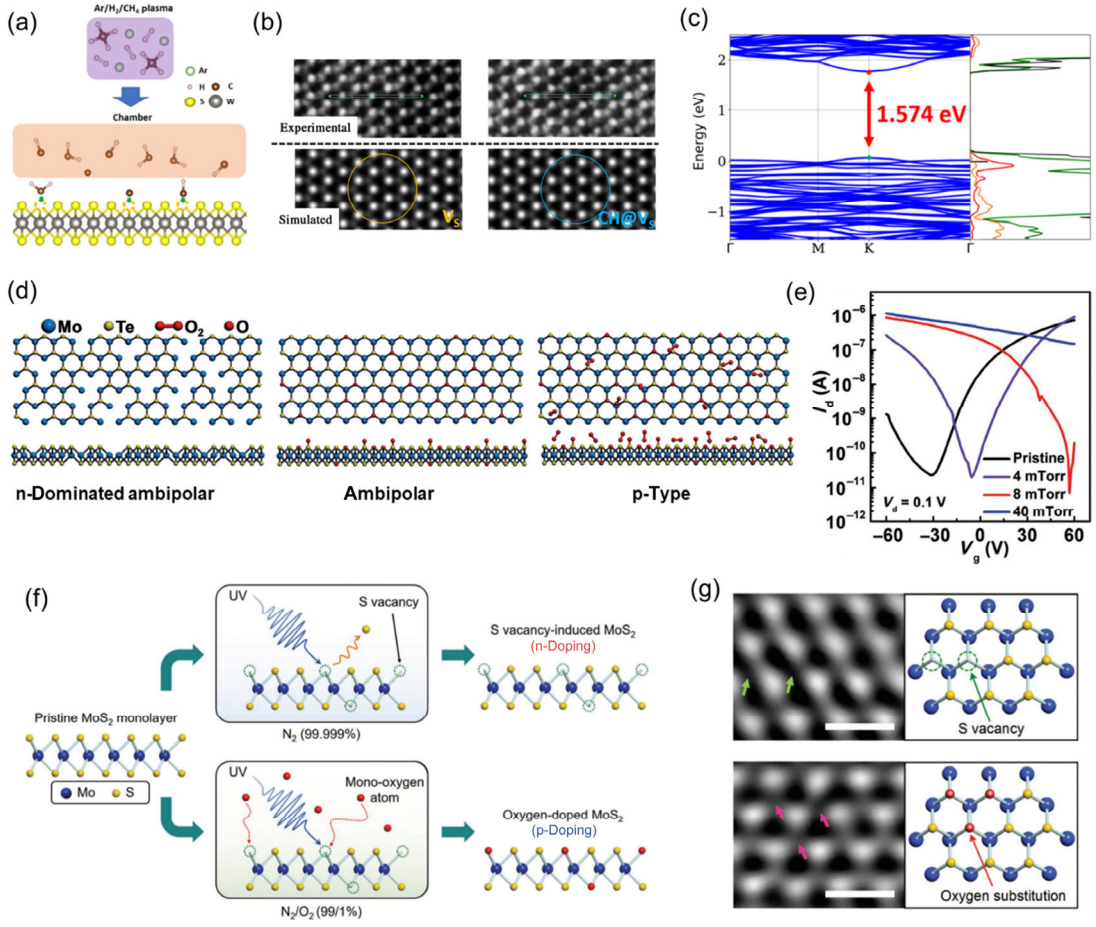

Figure 4 Postgrowth substitutional doping of TMDCs by low energy plasma treatment, thermal diffusion, and photon assistance. (a) Schematic diagrams of p-type doping WS_2 by plasma treatment of CH-groups. Reproduced with permission from Ref. [97], © The Authors 2019. (b) Experimental (top) and simulated (bottom) atomic-resolution HAADF-STEM images of a S monovacancy and a CH substitutional dopant on S sites of WS_2. Reproduced with permission from Ref. [97], © The Authors 2019. (c) Simulations band structure and DOS of WS_2 with CH on S sites. Reproduced with permission from Ref. [97], © The Authors 2019. (d) Schematic mechanism of thermal diffusion doping for $MoTe_2$ under O_2 atmosphere. Reproduced with permission from Ref. [96], © WILEY-VCH Verlag GmbH & Co. KGaA 2017. (e) Transfer curves of the O-doped $MoTe_2$ FETs at different vacuum levels. Reproduced with permission from Ref. [96], © WILEY-VCH Verlag GmbH & Co. KGaA 2017. (f) Schematic diagrams of the proposed mechanism on UV light-assisted doping under N_2 atmosphere (top) and N_2/O_2 atmosphere (bottom). Reproduced with permission from Ref. [76], © WILEY-VCH Verlag GmbH & Co. KGaA 2020. (g) Filtered annular dark field scanning transmission electron microscopy images (left) and schematic diagrams (right) of S vacancies and O substitutional dopants in MoS_2. Reproduced with permission from Ref. [76], © WILEY-VCH Verlag GmbH & Co. KGaA 2020.

treatment mentioned above. To confirm the p-type doping result in theory, the simulations of band structures and density of states (DOS) of WS_2 with CH on S sites were conducted (Fig. 4(c)), which shows a decreased bandgap of 1.574 eV (bandgap of pristine WS_2 = 1.791 eV) and higher acceptor level compared with the original valence band of WS_2.

Another complementary metal-oxide-semiconductor compatible substitutional doping method is thermal diffusion for which the doping process is carried out with high temperature annealing in an impurity atmosphere. In this case, local atoms could absorb the heating energy and then leave the material, which generates vacancies that would be occupied by foreign impurity atoms to finish the substitutional doping process. During thermal diffusion, the doping temperature should be lower than the self-decomposition temperature of pristine material to ensure its lattice integrity. A n-type thermal diffusion doping of WS_2 was carried out under 550 °C, which is lower than the growing temperature of WS_2 (750–850 °C) [105]. Besides, Qu et al. realized a O_2 thermal annealed p-type doping of $MoTe_2$ with two kinds of doping mechanisms, i.e., substitutional doping and surface charge transfer, as shown in Fig. 4(d) [96]. Oxygen first acted as substitutional dopants to fill in the Te vacancies, and then adsorbed on the surface of $MoTe_2$ to perform the surface charge transfer doping, which will be discussed in the following section. The conduction type of the O-doped $MoTe_2$ was changed from n-dominated ambipolar to p-type with the control of vacuum levels (Fig. 4(e)).

Except for the postgrowth substitutional doping methods mentioned above, substitutional doping with photon assistance is another alternative for TMDCs. Different from the traditional doping methods, photon-assisted substitutional doping uses light to provide energy for atom dissociation and impurity substitution. The doping type is determined by the type of dopant gas and the doping level could be controlled by concentration of dopant gas, exposure time, and light wavelength and power [72, 104]. In 2020, a UV light-assisted doping process for MoS_2 was carried out as shown in Fig. 4(f) [76]. Under UV light in N_2 and N_2/O_2 atmosphere, S vacancies and O substitutional dopants were clearly exhibited by filtered annular dark field scanning transmission electron microscopy (ADF-STEM) images (Fig. 4(g)), that led to n-type and p-type doping results, respectively.

2.3 Surface charge transfer

When a semiconductor material is exposed to a non-vacuum environment, some chemicals would adsorb on its surface and exchange charges with the host material. For bulk materials, adsorbates only affect their surface and have little influence on the intrinsic properties, however, for two-dimensional materials, these charge exchanges would change their charge distribution, energy band, and doping types due to their ultrahigh specific surface area [116]. The doping type could be predicted by the relative position between the redox potential (or work function) of adsorbates as well as the chemical potential of TMDCs [55]. When the redox potential of adsorbates is below the Fermi-level of TMDCs, electrons would transfer from TMDCs to adsorbates, which contribute to hole accumulations in TMDCs, i.e., p-type doping. On the contrary, it would form a n-type doping. According to the difference in implementation, the surface charge transfer doping strategy could be divided into two methods, i.e., surface adsorption and surface deposition/coating. Based on these methods, various doping chemicals along with their p-/n-type modulation properties were summarized in Table 2, that would discuss in detail as following.

2.3.1 *Surface adsorption*

In the air, the main ambient components such as H_2O and O_2

Table 2 A summary of typical doping chemicals and their properties for the surface charge transfer doping of TMDCs

Dopant	Doping type	Method	Material	Concentration (cm^{-2})	Stability	References
H_2O & O_2	p-Type	Surface adsorption	MoS_2, WSe_2, $MoTe_2$	—	Stable	[41, 117]
NO_2	p-Type	Surface adsorption	MoS_2, WSe_2	2.2×10^{12}	Unstable	[118, 119]
MoO_x	p-Type	Deposition	MoS_2, WSe_2	—	Stable	[120]
WO_x	p-Type	Oxidation by plasma or laser	WSe_2	10^{11}–10^{12}	Stable	[70, 121, 122]
Au, Ag, Pd, Pt	p-Type	Deposition	MoS_2	—	Stable	[123]
$TiCl_4$, $AuCl_3$	p-Type	Spin-coating	MoS_2, $MoSe_2$	10^{12}–10^{13}	Unstable	[124–131]
HCl	p-Type	Dipping	$ReSe_2$	10^{10}–10^{11}	Stable	[132]
$(NH_4)_2S$	p-Type	Soaking	WSe_2	—	Unstable	[133]
4-NBD	p-Type	Dipping	WSe_2	—	Unstable	[134]
TCNQ, F_4TCNQ	p-Type	Drop-casting	MoS_2	—	Stable	[135]
OTS	p-Type	Dipping	MoS_2, WSe_2	10^{11}	Unstable	[136]
NH_3	n-Type	Surface adsorption	MoS_2	—	Stable	[119]
K, Al, Y	n-Type	Deposition	MoS_2, WSe_2, $MoTe_2$	2.5×10^{12}	Unstable	[123, 137, 138]
Cs_2CO_3	n-Type	Deposition	MoS_2	3.5×10^{11}	Stable	[139]
Al_2O_3	n-Type	Deposition	$MoTe_2$	1.2×10^{12}	Stable	[140, 141]
KI	n-Type	Spin-coating	MoS_2	10^{12}	Stable	[142]
LiF	n-Type	Dipping	WS_2	—	Stable	[143]
N_2H_4	n-Type	Dipping	WSe_2	6×10^{12}	Unstable	[144–146]
BV	n-Type	Spin-coating	MoS_2, $MoTe_2$, WSe_2	10^{12}–10^{13}	Stable	[96, 125, 128, 147, 148]
DCE	n-Type	Dipping	MoS_2, WS_2	9.2×10^{12}, 6.0×10^{11}	Stable	[149]
DETA	n-Type	Vapor treatment	WSe_2	—	Stable	[134]
CTAB	n-Type	Dipping	WSe_2	—	Stable	[150]
PEI	n-Type	Dipping	MoS_2, WSe_2	—	Stable	[151, 152]
APTES	n-Type	Dipping	MoS_2, WSe_2	10^{11}	Unstable	[136]

would adsorb on TMDCs and influence their conduction types. In the characterization of doping result, photoluminescence (PL) spectrum is an effective method because PL peak intensities and positions would be regulated by the carrier distribution [42]. With H_2O and O_2 adsorbates, the PL spectra demonstrated a significant intensity enhancement for MoS_2 and an opposite change for WSe_2 (Figs. 5(a) and 5(b)) that could be specifically explained through the carrier recombination theory [41, 42]. The carrier recombinations consist of nonradiative recombination and radiative recombination (PL spectrum) which is further divided into exciton recombination (X^0) and trion recombination ($X^{+/-}$). The probabilities of these carrier recombinations would alter with the change of doping levels and eventually determine the peak intensity of PL spectra (Figs. 5(c) and 5(d)). When H_2O and O_2 were adsorbed on the surfaces of MoS_2 and WSe_2, the PL spectra of MoS_2 were enhanced with the mitigation of its n-type doping level, while the PL spectra of WSe_2 were weakened with the aggravation of its p-type doping level. Moreover, the relative PL peak intensities of two radiative recombinations (X^0 and $X^{+/-}$) would vary with the doping levels. Therefore, the main PL peak of MoS_2 and WSe_2 shifted along with the change of doping levels. Utilizing the p-type doping effect of H_2O and O_2 adsorption, a reversible doping of $MoTe_2$ could be realized by electrothermal annealing, that modulate the adsorption and desorption processes of H_2O and O_2 [117]. When $MoTe_2$ was annealed in vacuum, H_2O and O_2 were desorbed and refreshed the original conduction type of $MoTe_2$ (n-type) (procedure 1 to 2 in Fig. 5(e)), then H_2O and O_2 adsorption would spontaneously re-doped the $MoTe_2$ after exposing the samples in the air (procedure 2 to 3 in Fig. 5(e)). In addition to the doping of H_2O and O_2, nitrogen compounds of NO_2 and NH_3 present p-type and n-type doping results for TMDCs (Figs. 5(f) and 5(g)), respectively, owing to the strong oxidizing property of NO_2 and reducing property of NH_3 [118, 119].

2.3.2 *Surface deposition/coating*

Besides gas adsorptions discussed above, the doping process could also be achieved by artificial deposition or coating of chemicals on the surfaces of TMDCs. A variety of chemicals could act as donors (n-type dopants) or acceptors (p-type dopants) for TMDC doping such as metals [123, 137, 138], metal oxides [70, 121, 139–141], metal halide [125–130], organic molecules [125, 134–136, 146, 149, 150, 152], etc. Surface deposition/coating has the advantages of patterned doping capability, relative low doping temperature, and little crystal damage [129, 133, 134, 153]. However, the instability and poor process compatibility of some surface charge transfer dopants would restrict its real applications [137].

For the deposition doping process, Fang et al. evaporated alkali metal K onto the surfaces of MoS_2 and WSe_2 in a vacuum chamber (Fig. 6(a)) [137]. The strong reducibility of K provided extra electrons and eventually realized an almost degenerate n-type doping result (2.5×10^{12} cm^{-2}) (Fig. 6(b)). Similar doping process could be found in n-type doping metals (Al, Y) and p-type doping metals (Au, Ag, Pd, and Pt) for TMDCs [123, 138]. However, some metals are unstable since they are highly active and easy to be oxidized in the air, which requires extra protection through layer passivation. Different from the instable metals, a series of stable metal oxides and carbonates are chosen as dopants for TMDCs doping, for instance, p-type dopants of Mo and W oxides [70, 120–122], as well as n-type dopants of Cs_2CO_3 and Al_2O_3 [96, 139–141]. For Al_2O_3 doped TMDCs, the n-type doping induced by Al_2O_3 deposition results from the O vacancies existing at the interface and the methyl group dissociated from the depositing precursor, which created donor states near the conduction band edge of $MoTe_2$ (Fig. 6(c)). In addition, the deposition of Al_2O_3 could also lower the Schottky barrier height and improve the contacts between $MoTe_2$ and electrodes through the tunneling effect (Fig. 6(d)). It should be mentioned that using O_2 plasma or laser illumination would lead to the surface self-oxidization of TMDCs, which presents equivalent effects to the surface charge transfer doping of metal oxides deposition [70, 121, 122].

Another approach to carry out the surface charge transfer doping is spin-coating or dipping chemical solutions on the surfaces of TMDCs, in which it is simple and easy to apply a patterned doping with mask-assisted process (Fig. 6(e)). Among the doping chemicals, Lewis acid is a series of universal p-type doping solutions that could react with TMDCs to form 2D complexes and modify their Fermi levels [131]. One of the Lewis acids, $AuCl_3$, is the most commonly used for the p-type doping process (Fig. 6(f)) [124–130]. $AuCl_4^-$ ions in $AuCl_3$

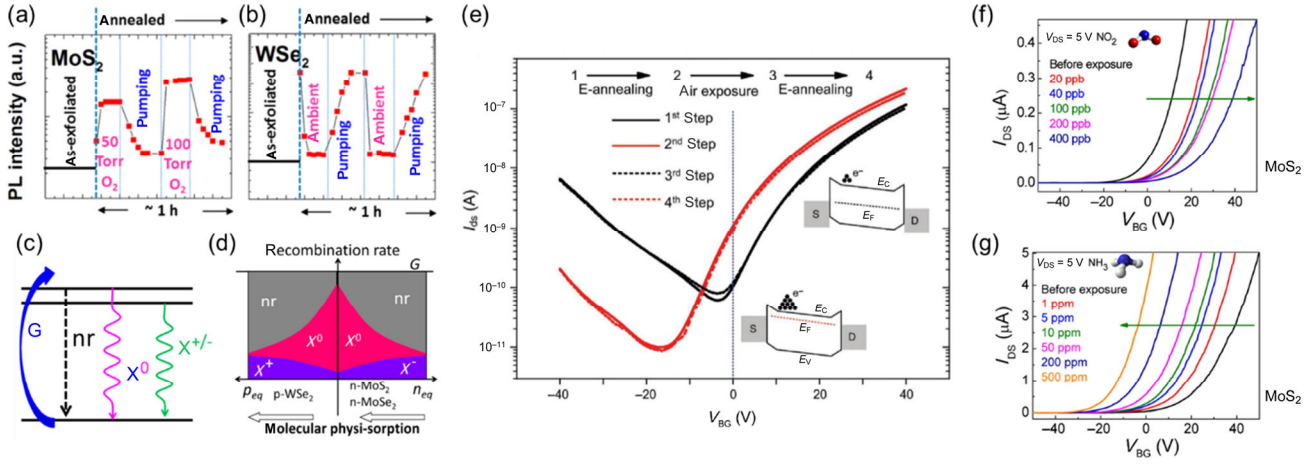

Figure 5 surface charge transfer doping of TMDCs by adsorbing gas molecules. (a) and (b) Modulation of the PL intensities of monolayer MoS_2 and WSe_2 as a function of H_2O and O_2 adsorbing time. Reproduced with permission from Ref. [41], © American Chemical Society 2013. (c) and (d) Schematic mechanism of PL intensity changes of TMDCs by adsorbing H_2O and O_2. Reproduced with permission from Ref. [41], © American Chemical Society 2013. (e) Transfer curves of $MoTe_2$ FET before and after electrothermal annealing proved its reversible doping. Insert is the energy band structures of MoS_2 FET before and after doping. Reproduced with permission from Ref. [117], © WILEY-VCH Verlag GmbH & Co. KGaA 2018. (f) and (g) Transfer curves of p- and n-type doping MoS_2 FETs doped by NO_2 and NH_3, respectively. Reproduced with permission from Ref. [119], © American Chemical Society 2014.

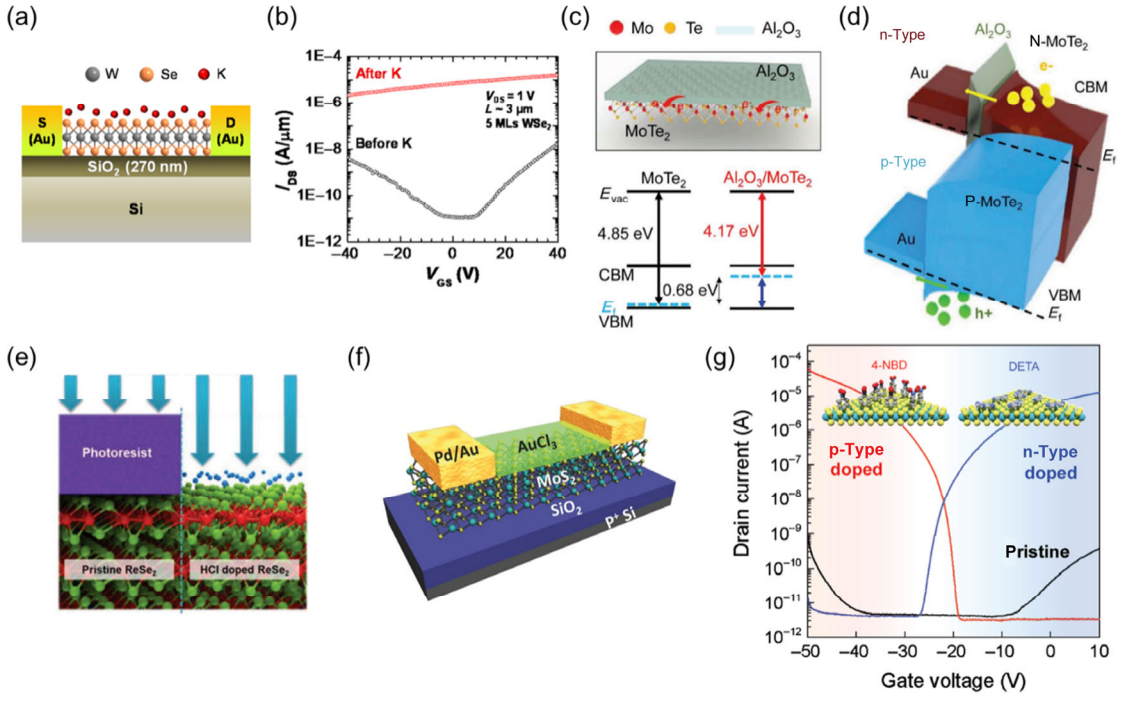

Figure 6 Surface charge transfer doping of TMDCs by deposition/coating. (a) Schematic diagram of n-type doping of WSe_2 FET by depositing K on its surface. Reproduced with permission from Ref. [137], © American Chemical Society 2013. (b) Transfer curves of WSe_2 FET before and after K deposition. Reproduced with permission from Ref. [137], © American Chemical Society 2013. (c) Schematic diagrams of electron transfer from AL_2O_3 to $MoTe_2$ and the energy band of $MoTe_2$ before and after Al_2O_3 deposition. Reproduced with permission from Ref. [140], © WILEY-VCH Verlag GmbH & Co. KGaA 2019. (d) Three-dimensional (3D) energy band diagrams of $MoTe_2$/Au contacts before (blue) and after (dark red) Al_2O_3 deposition. Reproduced with permission from Ref. [140], © WILEY-VCH Verlag GmbH & Co. KGaA 2019. (e) Schematic diagram of HCl patterned doping of $ReSe_2$ with mask assistance. Reproduced with permission from Ref. [132], © The Authors. Published by WILEY-VCH Verlag GmbH & Co. KGaA 2019. (f) Schematic diagram of p-type MoS_2 FET doped by $AuCl_3$. Reproduced with permission from Ref. [126], © WILEY-VCH Verlag GmbH & Co. KGaA 2016. (g) Transfer curves of 4-NBD (p-type) and DETA (n-type) doped WSe_2 FET, respectively. Reproduced with permission from Ref. [134], © WILEY-VCH Verlag GmbH & Co. KGaA 2019.

solution would capture the electrons in TMDCs, then the Fermi-level of TMDCs moves to its valence band and leads to the p-type doping result [154]. In addition to metal chlorides, other inorganic p-type doping solutions mainly include HCl [132] and $(NH_4)_2S$ [133], while inorganic n-type doping solutions consist of LiF [143] and KI [142]. What's more, surface treatment doped by organics is also an effective method to change the electric properties of TMDCs. For example, $-CH_3$ containing organics are often used as acceptors because of their positive pole to withdraw electrons from host materials [136], and $-NH_2$ containing organics are donors that have long electron pairs to supply electrons to host materials [134, 136, 144–146, 152]. Applicable p-type organic dopants are 4-NBD, OTS, TCNQ, and F_4TCNQ [134–136], and n-type organic dopants for TMDCs are BV, DCE, DETA, N_2H_4, APTES and CTAB [96, 125, 128, 134, 136, 144–150]. Figure 6(g) illustrates the general p- and n-type transfer curves of WSe_2 FETs after patterned doping of 4-NBD and DETA, respectively [134]. However, the chemical solutions used for surface charge transfer doping also face the same problem of chemical instability. Therefore, it is worth noting to conduct further studies to achieve a stable surface during the charge transfer doping process.

2.4 Chemical intercalation

Different from the strong chemical bonds of nonlayered semiconductor materials, TMDCs are stacked layer by layer with van der Waals force and could be easily inserted through atoms, ions as well as molecules. Chemical intercalation could be executed by three kinds of methods: electrochemical intercalation, vapor phase intercalation, and liquid-phase intercalation [155]. With chemical intercalation, the molecular structure, energy band, and charge distribution of TMDCs would be changed owing to the strong interlayer interactions and charge exchanges, leading to the phenomena like doping effect [156, 157], phase change [9, 158, 159], superlattice [16], and superconductivity [160, 161]. In the aspect of p-/n-type modulation, some intercalants have more outer electrons than the host lattices and act as donor-type species (i.e., n-type doping) such as alkaline and alkaline-earth metals, and some others have fewer outer electrons and act as acceptors to withdraw electrons (i.e., p-type doping) like H_2SO_4 [155, 162]. In this vein, Cui and coworkers intercalated some zerovalent metal atoms (Ag, Au, Co, Cu, Fe, In, Ni, and Sn) into the Bi_2Se_3 interlayers by the disproportionation redox reaction [163]. Inspired by this method, the p-type and metallic-type (m-type) doping of SnS_2 by Cu and Co atoms intercalation were carried out respectively [156]. In combination with the defect-related n-type SnS_2 and the mask-assisted patterning process, this doping method realized different conduction types (n-type, p-type, and m-type) as well as junctions (p-n junction, m-p junction, and m-n junction) (Fig. 7(a)). The doping type of SnS_2 could be easily distinguished with the sample colors under optical microscopy observation as shown in Figs. 7(b)–7(d). To compare their conductivities, the sheet resistances and transfer curve (Cu-SnS_2) were measured with few-layer graphene as a metallic conducting reference. The characterization results show a clearly metallic conduction for Co-SnS_2 and p-type conduction for Cu-SnS_2 respectively (Figs. 7(e) and 7(f)). Besides, this doping method is quite universal for other TMDCs including group IVB, VB, and VIIB. Nevertheless, the controllable intercalation-induced p-/n-type modulation is still challengeable due to the strong interlayer interactions between intercalants and host lattices that easily

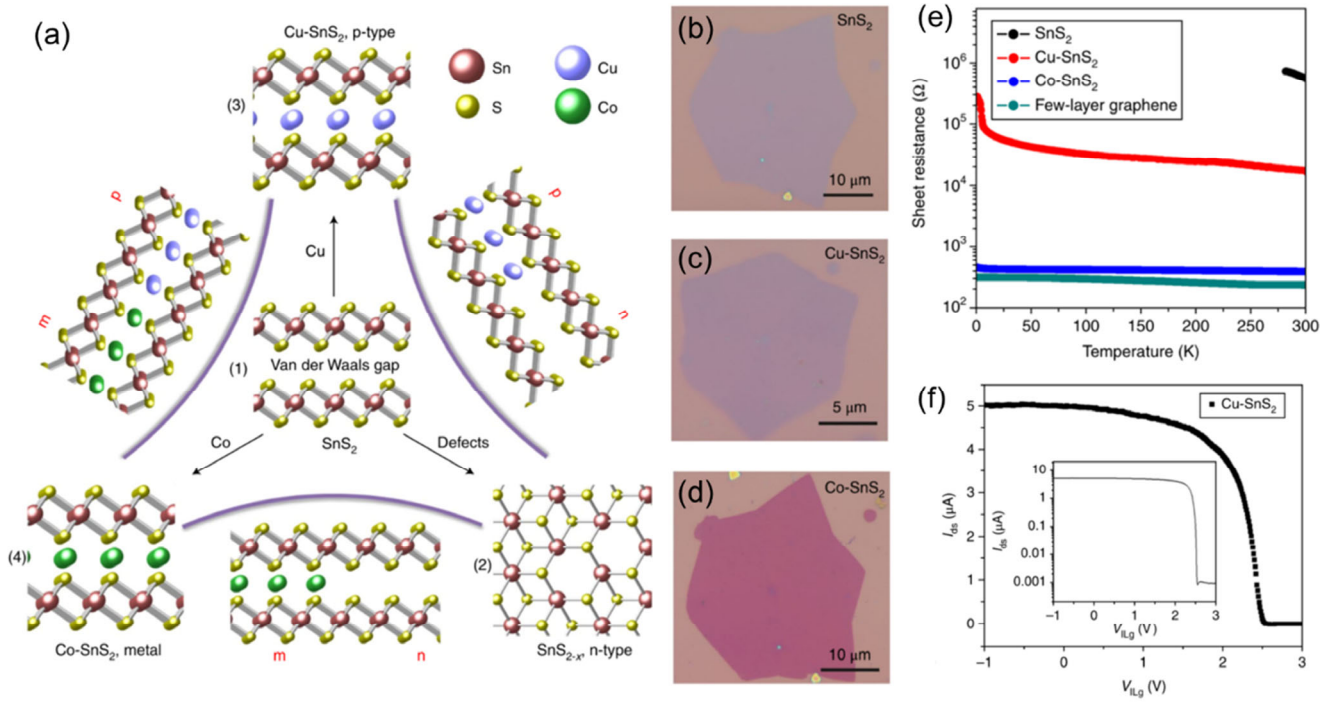

Figure 7 Realization of n-type, p-type, and metallic-type conductions from the parent material (SnS_2) by Cu and Co intercalation. (a) Schematic diagram of n-type SnS_2 with defects, p-type SnS_2 with Cu intercalation, metallic SnS_2 with Co intercalation, and their junctions. Reproduced with permission from Ref. [156]. © Macmillan Publishers Limited, part of Springer Nature 2018. (b)–(d) Optical images of (b) SnS_2, (c) Cu-SnS_2, and (d) Co-SnS_2. Reproduced with permission from Ref. [156]. © Macmillan Publishers Limited, part of Springer Nature 2018. (e) Sheet resistances of SnS_2 (black), Cu-SnS_2 (red), Co-SnS_2 (blue) and few-layer graphene (green) as a function of temperature which showed a good metallic conductivity of Co-SnS_2 and appropriate semiconductor conductivities of SnS_2 and Cu-SnS_2. Reproduced with permission from Ref. [156]. © Macmillan Publishers Limited, part of Springer Nature 2018. (f) Transfer curves of Cu-SnS_2 FET with ionic liquid gated showing a typical p-type conducting behavior. Inset: transfer curve of this device on the logarithmic scale. Reproduced with permission from Ref. [156]. © Macmillan Publishers Limited, part of Springer Nature 2018.

lead to phase or superconducting transition. Thus, this kind of doping strategies need much further studies to realize a more moderate doping way.

2.5 Electrostatic modulation

Utilizing the field-effect of metal-insulator-semiconductor (MIS) structure, the electrons and holes could be attracted to the surface of a semiconductor channel by gate voltage [11]. For the device channel constructed by bulk semiconductor materials, the gate voltage could only control the carrier distribution with an extremely thin thickness (a magnitude of nanometer) [164, 165]. By contrast, the carrier distribution of a 2D material could fully be controlled by the gate voltage of which modulation levels are equivalently referred to as the doping effect due to its sub-nanometer thickness [166]. Compared with the chemical doping of TMDCs discussed above, this equivalent doping strategy has the advantages of flexible designing multifunctional devices and accurate controlling of doping levels.

2.5.1 *Volatile electrostatic modulation*

The easiest method to realize electrostatic modulation for 2D materials is achieved by applying gate voltages on graphene devices [167, 168]. Subsequently, the fabrication of WSe_2 FET based on double local gates were reported [169–173]. As shown in Fig. 8(a), two local gates were buried under the WSe_2/h-BN structure and could control the p- and n-type levels of WSe_2 through applying gate voltages [173]. When applying negative (positive) gate voltages, the WSe_2 channel was electrostatically p-type (n-type) doped by the field effect. Therefore, the p-p, p-n, n-p, n-n junctions could be flexibly converted. Taking the p-n junction as an example, it would be switched on (10^{-4} A) at drain-source bias of 5 V and turned off (10^{-9} A) at drain-source bias of –5 V, as shown at the top right corners in Figs. 8(b) and 8(c), respectively. In 2D material FETs, various isolators have been investigated such as thermally grown SiO_2, high-k oxides (Al_2O_3, HfO_2, etc.), crystalline CaF_2, and 2D h-BN [174–178]. In general, an isolator with large permittivity and bandgap could provide more induced holes or electrons which means a higher level p-/n-type modulation. Figure 8(d) illustrates the calculated leakage current properties of different insulators considering the theories of thermionic emission, Fowler-Nordheim (FN) tunneling and direct tunneling [174]. As can be seen in this figure, HfO_2 and crystalline CaF_2 have the lowest leakage currents that benefit from the highest permittivity of 25 and widest bandgap of 12.1 eV with defect-free interface.

Although local gate modulation shows a good doping result, it is only suitable for a few kinds of ambipolar TMDCs. The doping is still not enough for the unipolar TMDCs (MoS_2, $MoSe_2$, WS_2, etc.) because of its limited field-effect modulating capability. An effective way to increase the gate capacitance is to thin the dielectric layer. For the electrostatic modulation of unipolar TMDCs, an alternative approach is to use the ionic conductor which could control the carrier distribution of a device channel in a wide range by its mobile ions. Moreover, controlled by gate voltage, mobile ions shift close to the interface between the dielectric layer and channel, so as to decrease the equivalent thickness of dielectric layer to the magnitude of nanometers, thereby significantly enhancing the capability of field-effect modulation (Figs. 8(e) and 8(f)). Several groups achieved ambipolar conductions of MoS_2 by liquid ionic conductors [179–182]. However, the process using liquid ionic conductor is difficult to be industrialized.

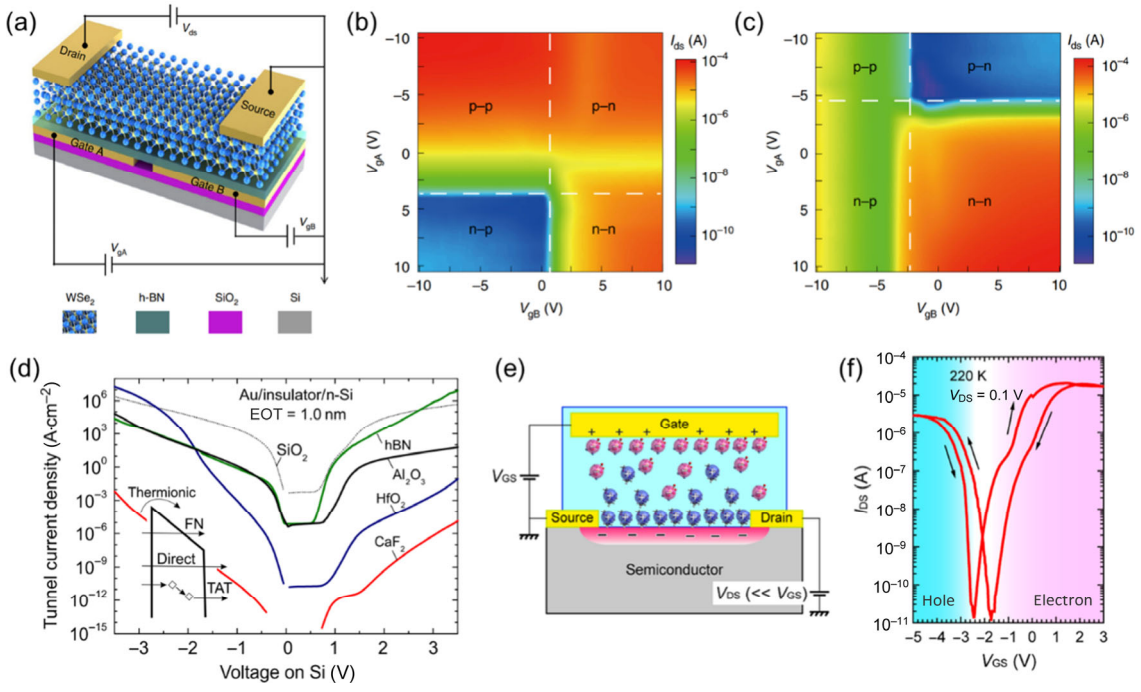

Figure 8 Volatile electrostatic modulation of TMDCs through local gates and ionic conductors. (a) Schematic diagram of WSe_2 FET controlled by two local gates. Reproduced with permission from Ref. [173], © The Author(s), under exclusive licence to Springer Nature Limited 2020. (b) and (c) Drain current mapping as a function of two local gates in (a) at V_{DS} = 5 V (b) and V_{DS} = –5 V (c), respectively. Reproduced with permission from Ref. [173], © The Author(s), under exclusive licence to Springer Nature Limited 2020. (d) Leakage currents through metal-insulator-semiconductor structures with different insulators calculated by the Wentzel–Kramers–Brillouin (WKB) approach (EOT = 1 nm) considering thermionic emission, Fowler-Nordheim tunneling and direct tunneling. The rap-assisted tunneling (TAT) for defective insulators is not accounted for in this model. Reproduced with permission from Ref. [174], © The Author(s) 2020. (e) Schematic diagram of MoS_2 modulated by liquid ionic conductor at $V_{DS} \ll V_{GS}$. Reproduced with permission from Ref. [181], © American Chemical Society 2013. (f) Transfer curve of the device in (f) with a full-cycle gate sweep at V_{DS} = 0.1 V. Reproduced with permission from Ref. [181], © American Chemical Society 2013.

From 2018, two solid ionic conductors (LaF_3 and $LiTaO_3$) were reported to modulate MoS_2 which solve the problem of process compatibility and demonstrate the potential capability for the device applications of ionic conductors [183–185].

2.5.2 *Non-volatile electrostatic modulation*

Regarding the electrostatic modulation methods aforementioned, the need of continuous gate voltage to maintain the doping effect induces an additional energy consumption. A possible solution is the non-volatile memory mechanisms according to the floating gate modulation [186–195] and space charge polarization [196–199]. For the floating gate modulation, charge carriers in TMDCs tunnel from device channel to the floating gate or isolator trap states through a pulse gate writing voltage (sometimes under light illumination) and cannot move back, therefore achieving non-volatile doping result. Two typical floating gate structures are shown in Figs. 9(a) and 9(b). Taking the device structure in Fig. 9(b) as an example, the UV illumination would excite the photo-induced electron-hole pairs in $MoTe_2$ [186]. Excited electrons (holes) would migrate from the $MoTe_2$ to h-BN/SiO_2 interface through tunneling effect under a high positive (negative) voltage pulse on back gate. A large range of doping level was presented by the transfer curves as shown in Fig. 9(c). Furthermore, this kind of doping could also be achieved by focused electron beam under pulse gate writing voltages (Fig. 9(d)) [200]. During the electron-beam exposure with low energies (1–2 keV), electron–hole pairs were excited in the bottom h-BN layers, then hot electrons (holes) drifted to the Si substrate at positive (negative) gate voltages and were trapped in h-BN defects near the h-BN/SiO_2 interface, eventually causing the non-volatile p-type (n-type) doping effects. This patterned doping precision could be achieved as high as 200 nm (Fig. 9(e)).

Besides the floating gate modulation, space charge polarization is also an alternative approach that could be subdivided into two kinds of mechanisms: ferroelectric polarization and superionic phase transition. Figure 9(f) depicts a ferroelectric-based device structure, in which the ferroelectric domains would be pre-polarized to an arbitrary pattern by a scanning probe and served as a template for the following doping of the $MoTe_2$ channel layer. In Fig. 9(g), the $MoTe_2$ was doped to the p-type region (left) and n-type region (right), thus forming a p-n homojunction which could be demonstrated in the phase image of piezoresponse force microscopy (PFM). Different from the ferroelectric polarization, AgI dielectric layer could carry out a non-volatile p-/n-type modulation by temperature-induced phase transition (sharp change in ionic conductivity) (Fig. 9(h)). When applying negative back gate voltage at phase transition temperature (147 °C), Ag^+ ions migrated close to back gate and electrostatically n-type doped the WSe_2 channel, and then achieved the non-volatile electrostatic modulation (Fig. 9(i)).

2.6 Dielectric interface engineering

Different from the aforementioned p-/n-type modulation strategies, for dielectric interface engineering, the interface is supposed to be a special factor that could influence the doping levels of TMDCs through the interface interactions between dielectrics and TMDCs. Taking MoS_2 on Si/SiO_2 substrate as an example, the proximity of the trapped charges captured by the dangling bonds of SiO_2 substrate would lead to band tails and localized states of MoS_2, thus provoking fluctuations in its conduction band (Fig. 10(a)) [52]. This effect is equivalent to the Fermi-level

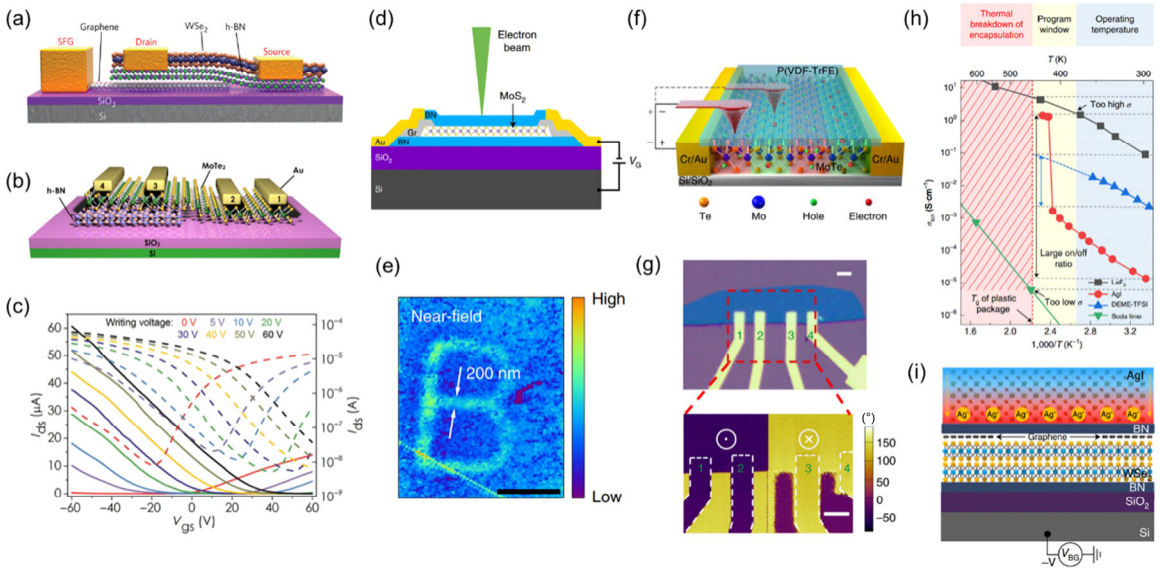

Figure 9 Non-volatile electrostatic modulation of TMDCs. (a) Schematic diagram of non-volatile electrostatic modulation using the device structure of WSe_2/h-BN/graphene SFG-FET. Reproduced with permission from Ref. [190], © Macmillan Publishers Limited, part of Springer Nature 2017. (b) Schematic diagram of non-volatile electrostatic modulation using the device structure of $MoTe_2$/h-BN and UV illumination. Reproduced with permission from Ref. [186], © The Authors, some rights reserved; exclusive licensee American Association for the Advancement of Science. No claim to original U.S.Government Works. Distributed under a Creative Commons Attribution NonCommercial License 4.0 (CC BY-NC) 2019. (c) Transfer curves of the device between the electrodes 3 and 4 in (b) after the non-volatile p-type doping at different writing voltages under UV illumination. Reproduced with permission from Ref. [186], © The Authors, some rights reserved; exclusive licensee American Association for the Advancement of Science. No claim to original U.S.Government Works. Distributed under a Creative Commons Attribution NonCommercial License 4.0 (CC BY-NC) 2019. (d) Cross-sectional view of electron-beam doping in a BN-encapsulated monolayer MoS_2 FET with multilayer graphene contacts. (e) Transfer curves of monolayer MoS_2 FET after electron-bean exposure with different writing voltages (V_{SET}). Reproduced with permission from Ref. [200], © The Author(s), under exclusive licence to Springer Nature Limited 2020. (f) Schematic diagram of non-volatile electrostatic modulation of $MoTe_2$ FET by the patterned ferroelectric polarizations. Reproduced with permission from Ref. [196], © The Author(s), under exclusive licence to Springer Nature Limited 2020. (g) Optical micrograph of the device in (f) (top). PFM phase image of the device in the red dashed line to demonstrate the two opposite ferroelectric polarizations (bottom). Reproduced with permission from Ref. [196], © The Author(s), under exclusive licence to Springer Nature Limited 2020. (h) Comparison of ionic conductivities as a function of temperature which illustrates the sharp change in ionic conductivity. Reproduced with permission from Ref. [199], © The Author(s), under exclusive licence to Springer Nature Limited 2020. (i) Schematic diagram of non-volatile electrostatic modulation of the WSe_2 FET by superionic AgI at a negative gate voltage. Reproduced with permission from Ref. [199], © The Author(s), under exclusive licence to Springer Nature Limited 2020.

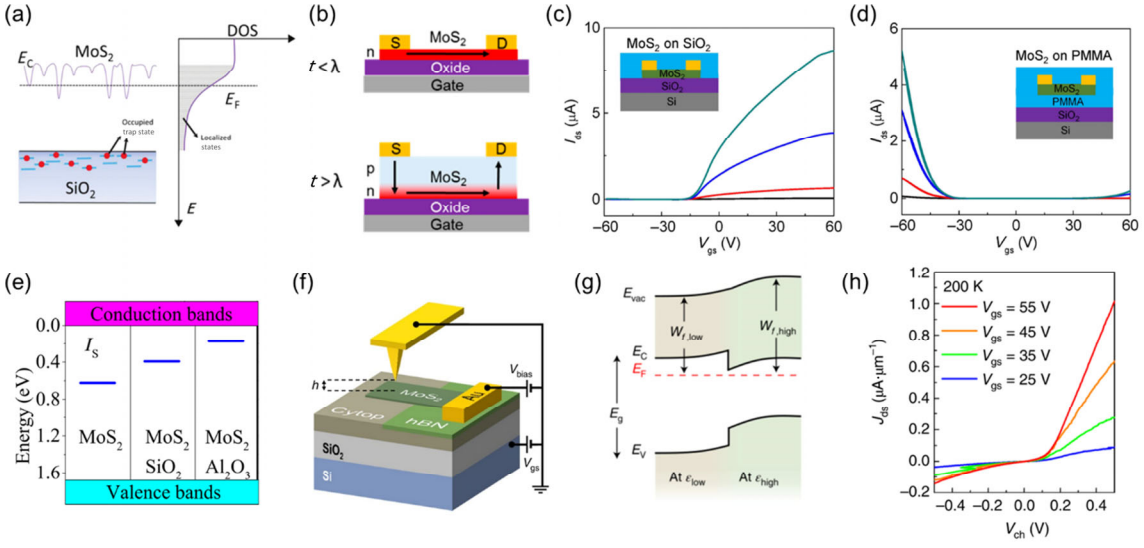

Figure 10 Influence of the interfaces between dielectrics and TMDCs. (a) Schematic diagram of the fluctuations and the band tail in the conduction band of MoS_2 thin films. Reproduced with permission from Ref. [52], © American Chemical Society 2011. (b) Schematic diagrams of MoS_2 on SiO_2 substrates with two thicknesses. The thin MoS_2 was all n-type doped by SiO_2 substrate and the thick one was partially n-type doped (bottom) by SiO_2 substrate. "t", thickness of MoS_2; "λ", n-type doping thickness of MoS_2 by the substrate. Reproduced with permission from Ref. [201], © American Chemical Society 2017. Transfer curves of MoS_2 FETs on (c) SiO_2 substrate and (d) PMMA substrate at different V_{DS}. Reproduced with permission from Ref. [15], © Macmillan Publishers Limited, part of Springer Nature 2018. (e) Calculated doping energy levels of I_S-doped MoS_2 on different substrates (left, with no substrate; middle, on SiO_2 substrate; right, on Al_2O_3 substrate). Reproduced with permission from Ref. [50], © American Physical Society 2017. (f) Schematic diagram of the Kelvin probe force microscopy (KPFM) measurement for a monolayer MoS_2 on CYTOP (left) and h-BN substrate (right). Reproduced with permission from Ref. [205], © The Author(s), under exclusive licence to Springer Nature Li mited 2019. (g) Energy band diagram of a MoS_2 on CYTOP (left) and h-BN substrate (right) acquired by KPFM measurement and calculation. Reproduced with permission from Ref. [205], © The Author(s), under exclusive licence to Springer Nature Limited 2019. (h) Output curves of the device at various V_{GS} under the temperature of 200 K. Reproduced with permission from Ref. [205], © The Author(s), under exclusive licence to Springer Nature Limited 2019.

approaching to the conduction band minimum and introduces n-type doping for the part of MoS_2 near the dielectric interface (Fig. 10(b)) [201]. To avoid or reduce the doping effect of substrate, several researchers spin-coated polymethyl methacrylate (PMMA) on SiO_2 substrate, separating therefore the MoS_2 and SiO_2. The MoS_2 FETs on the PMMA substrates displayed ambipolar or p-type conduction type (Figs. 10(c) and 10(d)), which is much different from the result (n-type) without PMMA layer [15, 201, 202]. Besides, the ionization energy of dopant would also be influenced by the substrate dielectric properties. Ma et al. studied the halogen (Cl, Br, and I) doping for MoS_2 on different substrates (without substrate, SiO_2 and Al_2O_3 substrates) through *ab-initio* calculation [50]. Taking I element in halogen as an example, the ionization energies of I_s-dopant tuned from deep energy level (0.63 eV for no substrate) to a shallow one (0.17 eV for Al_2O_3 substrate) along with the increase of substrate relative permittivity (Fig. 10(e)), which means that MoS_2 is more easily doped on the substrate with a high permittivity. The experiments of TMDCs doping on specific substrates have also been studied. A wide-range n-type doping of MoS_2 (from 3.6×10^{10} to 8.3×10^{12} cm^{-2}) was performed on phosphorus silicate glass (PSG) [203, 204]. Through the thermal and optical activation of PSG, the dipole induction of P_2O_5 was enhanced which motivated O atoms with a negative pole to hold the holes of MoS_2 at the interface region, resulting in n-type doping of MoS_2. Furthermore, Utama et al. transferred a monolayer MoS_2 atop the boundary of a h-BN flake on an amorphous fluoropolymer (CYTOP) film (Fig. 10(f)) [205]. These two substrates modulated the energy band of MoS_2 to a homojunction (Fig. 10(g)) and lead to a visible rectification characteristic at various V_{GS} under the temperature of 200 K (Fig. 10(h)).

3 Device applications of doping strategies

Based on the six kinds of p-/n-type modulation strategies aforementioned, a variety of TMDC-based semiconductor devices are prepared with enhanced performances and diverse functions. In this section, the working mechanisms and performance comparisons of typical electronic and optoelectronic devices based on these strategies, namely junction devices, FETs, photodetectors, and light-emitting diodes (LEDs) are discussed.

3.1 Energy band engineering

It is well known that the reality of a device function requires an elaborate design of energy band structure that is performed by p-/n-type modulation [206]. For energy band engineering in semiconductor devices, two kinds of junctions are the most essential structures, which are constructed by metal-semiconductor contact and semiconductor contact [34]. When a TMDC contacts with a metal (Fig. 11(a)), ohmic or Schottky contacts would be formed according to the tunable Fermi-level height compared with work function (metal) [33]. Figure 11(b) displays a n-type TMDC-based Schottky contact of which Fermi-level could be tuned away from or close to the conduction band to optimize the Schottky barrier and control the carrier transport paths between thermionic emission and tunneling [35]. On the one hand, the leakage current of a MoS_2 Schottky diode could be decreased through the extension of Schottky barrier width by lowering the Fermi-level [73]. On the other hand, the contact resistances of a device could be dramatically reduced through a heavily doping process, resulting in the improvement of the device performance [147]. As for the semiconductor junctions, two kinds of homojunctions (lateral and vertical junctions) could be formed by patterned p- and n-type doping process (Fig. 11(c)) [34, 206]. When a TMDC is

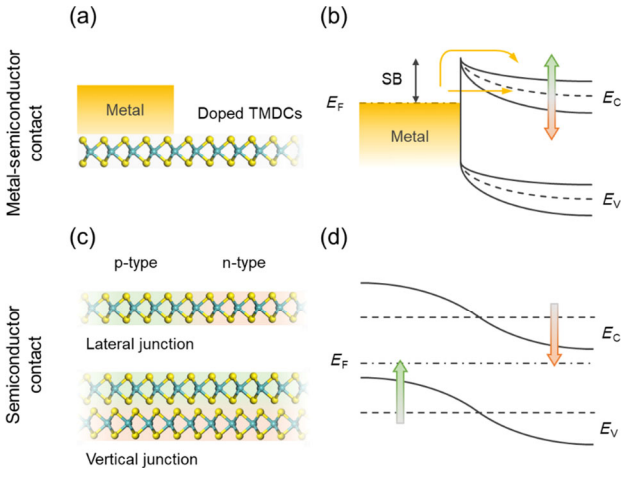

Figure 11 Band structure engineering based on p-/n-type modulation strategies. (a) and (b) Schematic diagram of metal-semiconductor contact and its energy band regulated by p-/n-type modulation. (c) and (d) Schematic diagram of two kinds of p-n junctions and energy band regulated by p-/n-type modulation. The p- and n-type TMDCs are filled with light orange and light green, respectively.

doped to p- and n-conduction types in two separate parts, the energy band of p-type TMDC rises up (green arrow in Fig. 11(d)) while the n-type one falls down (red arrow in Fig. 11(d)), and eventually forming a p-n junction. With the regulations and cascades of semiconductor and metal-semiconductor junctions, several typical electronic and optoelectronic devices could be fabricated, for instance, diodes, BJTs, FETs, photodetectors, etc., which would be discussed in detail in the following sections [11, 12, 58, 207].

3.2 Electronic and optoelectronic devices

3.2.1 *Electronic devices*

Owing to the distinctive layered crystal structures and properties, TMDCs have been attracted enormous interest in the fabrication of electronic devices, that could be divided into junction devices and FET devices. In this section, these two kinds of electronic devices based on p-/n-modulation are demonstrated to summarize their development and deliver some references and inspirations for the device functions and performances.

The basic two-terminal junction devices of TMDCs are p-n and Schottky diodes (Fig. 12(a)), that are constructed by semiconductor and metal-semiconductor contacts, respectively, aforementioned in the previous section. Beneficial from the defect-free van der Waals contact, tunable band gap, and p-/n-type modulation, TMDC-based diodes distinctly weaken the Fermi-level pinning effect and demonstrate a huge potential to follow the Schottky-Mott law, acting as a good candidate for the fabrication of ideal rectifiers [15, 44, 73, 208–210]. So far, the homojunction rectifiers fabricated by different doping strategies have been reported with high rectification ratios larger than 10^5 [73, 122, 189, 211]. Figure 12(b) depicts a typical rectification behavior of a rectifier doped by semi-floating gate (h-BN/half graphene/WSe_2 structure) electrostatic modulation [190]. Utilizing this rectification behavior, the negative input voltage was intercepted but the positive one passed through, which is applicable for the alternating current/direct current (AC/DC) conversion (Fig. 12(c)). Besides, the doped TMDC-based tunnel diode could also be fabricated which is helpful for the applications of microwave amplifying, high frequency switching (Fig. 12(d)) [128]. Through the $AlCl_3$ (p-type) and BV (n-type) surface charge transfer doping, the MoS_2 was

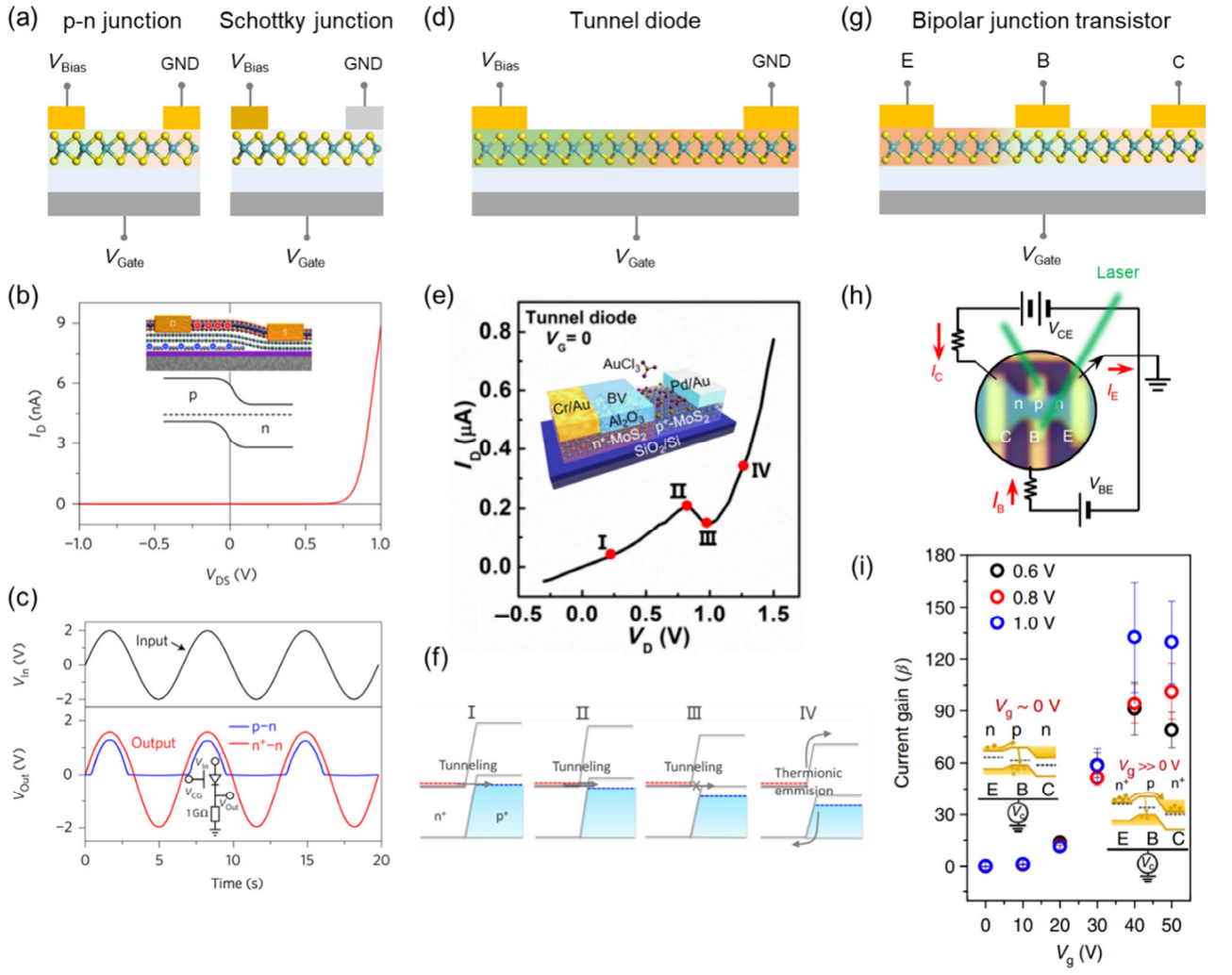

Figure 12 Junction devices based on p-/n-type modulation and their working modes. (a) Schematic diagram of two kinds of diodes based on p-n and Schottky junctions. (b) *I*–*V* curves of p-n junction diode after non-volatile electrostatic modulation. Reproduced with permission from Ref. [190], © Macmillan Publishers Limited, part of Springer Nature 2017. (c) Rectifying behaviors of the device in (b) at different states (p-n and n$^+$-n). Reproduced with permission from Ref. [190], © Macmillan Publishers Limited, part of Springer Nature 2017. (d) Schematic diagram of a tunnel diode. (e) *I*–*V* curve of tunnel diode with a negative differential resistance (NDR) behavior fabricated by surface charge transfer. Inset: schematic diagram of the doped MoS_2 tunnel diode. Reproduced with permission from Ref. [128], © AIP Publishing 2018. (f) Band diagrams and carrier transport paths for the MoS_2 tunnel diode at each specific drain bias corresponding to (e). Reproduced with permission from Ref. [128], © AIP Publishing 2018. (g) Schematic diagram of a bipolar junction transistor (BJT). (h) Circuit diagram with the common emitter (CE) configuration of the $MoTe_2$ n-p-n BJT doped by laser-induced surface charge transfer. © Spring Nature 2018. (i) Gate voltage-dependent current gain β with V_{CE} = 0.6, 0.8 and 1.0 V. Inset: energy band diagrams of $MoTe_2$ BJT with small *Vg* (left) and large *Vg* (right). Reproduced with permission from Ref. [54], © The Author(s), under exclusive licence to Springer Nature Limited 2018. The p- and n-type TMDCs in (a), (d), and (g) are filled with orange and green, respectively, and the doping levels are presented by the depth of filling colors.

modulated to a heavily doped p-n junction that the free electrons could pass directly through the band-to-band tunneling (BTBT) (I and II procedures in Figs. 12(e) and 12(f)). Along with the forward bias increasing, the energy band of p-type region would move up to block the BTBT carrier transport path (III procedures in Figs. 12(e) and 12(f)), and then occur the thermionic emission with a high forward bias (IV procedures in Figs. 12(e) and 12(f)). Except for the two-terminal junction devices, the doped TMDC-based BJT (Fig. 12(g)) were also reported with the doping strategies of surface charge transfer and electrostatic modulation [54, 212, 213]. Figure 12(h) shows a typical common emitter configuration of the $MoTe_2$ n-p-n BJT doped by laser-induced surface charge transfer [54]. Promoted by the gate voltage (> 40 V), the emitter and collector were further doped by electrostatic modulation (right inset energy band diagram in Fig. 12(i)), and eventually enhancing the current gain β as large as 150.

FET is a kind of devices that the electric channel is controlled capacitively by an electric field, of which typical device is MOSFET, a currently most basic unit of logic IC [214]. Facing the challenge of channel size scaling, TMDC-based FETs demonstrate potential approaches to continue the Moore's law in the prospective future due to their atomically thin layers [12, 207, 215]. Figure 13(a) illustrates the TMDC-based enhancement-mode n-/p-type MOSFET structures. When a TMDC FET is modulated to n-type (p-type) doping, it would be tuned on at a positive (negative) gate voltage and tuned off at a negative (positive) one (Fig. 13(b)). A variety of doped TMDC FETs have been studied to estimate the doping strategy and explore the device performances [55]. The relationship between carrier mobility and on/off ratio for the doped TMDC FETs has been summarized to analyze the current research state, as shown in Fig. 13(c). The filled and open symbols denote the electron (n-type) and hole (p-type) mobilities, respectively. It should be noted that the values of carrier mobilities are mainly extracted from two-terminal FET measurements with experimental

uncertainties. As can be seen in this relationship, a majority of doped TMDC FETs perform on/off ratios and mobilities ranging from 10^4–10^7 and 1–100 $cm^2 \cdot V^{-1} \cdot s^{-1}$, respectively. Different doping strategies are denoted by the symbol shapes, including intrinsic defect tailoring (square), substitutional doping (circle), surface charge transfer (upper triangle), chemical intercalation (lower triangle), and electrostatic modulation (diamond). It could be found that the TMDC FETs doped by surface charge transfer and substitutional doping exhibit better performance (close to the performed corner), while the electrostatic modulation is more moderate in doping level and more flexible in device design [81, 166, 216]. Besides, doped WSe_2 FETs perform better characteristics and are easier to convert charge polarities than most of other TMDCs in statistics.

Utilizing the doped FET structures, logic devices with various functions could be designed [217–219]. The basic and most used logic unit is inverter which is formed by p- and n-type FETs in series (Fig. 13(d)) [134]. Figure 13(e) illustrates the typical voltage transfer characteristic and the corresponding voltage gain of the inverter, which indicates that the only considerable power consumption is in the voltage level conversion procedure. Through a more complex cascades of doped TMDC FETs, more functional logic could be realized, such as NAND, NOR, XOR (Figs. 13(f) and 13(g)) [175], and even an innovatively reconfigurable logic device (Figs. 13(h) and 13(i)) [173].

3.2.2 *Optoelectronic devices*

Except for the application in electronic devices, TMDC doping has also been widely investigated in optoelectronic devices, for

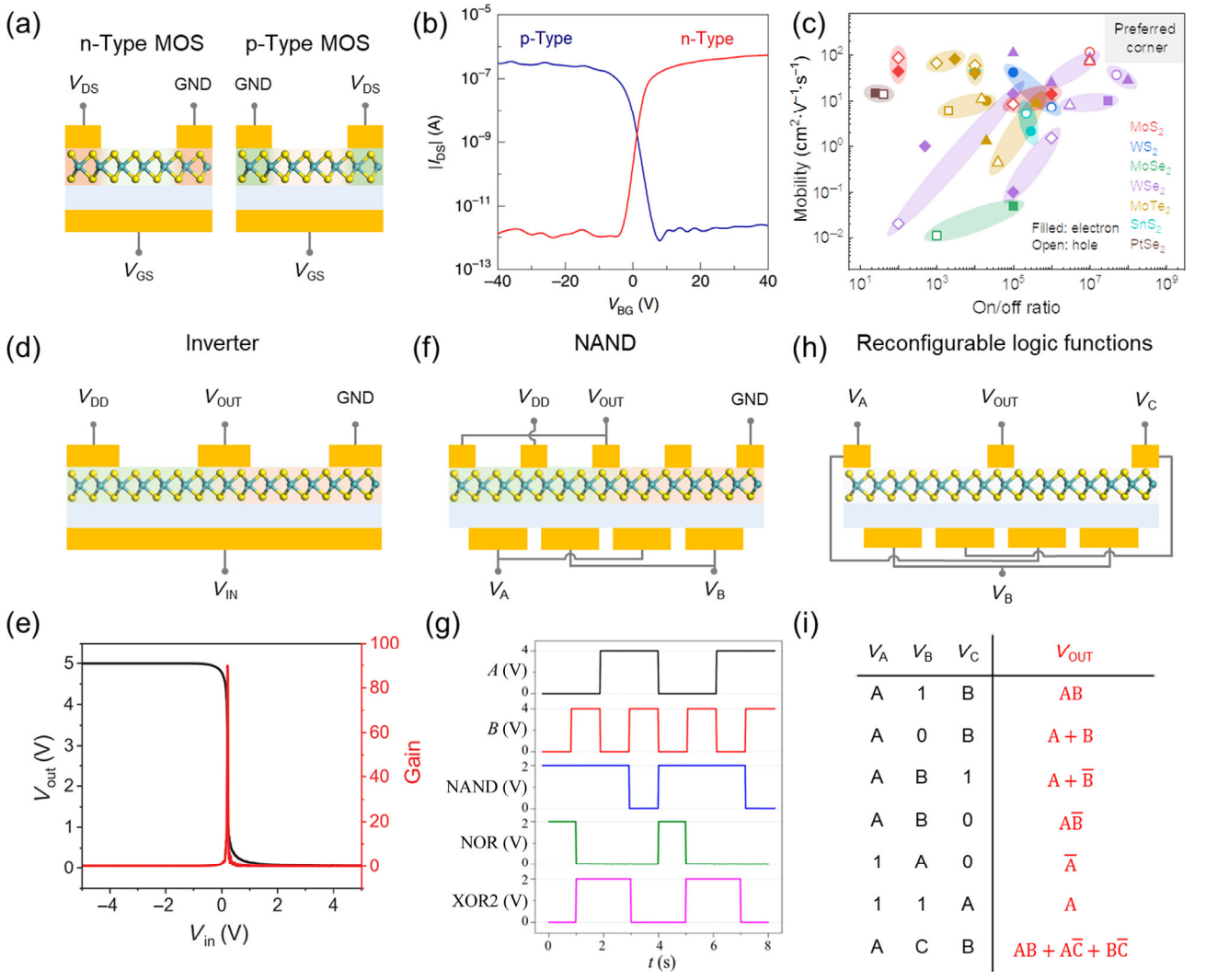

Figure 13 Field-effect transistors and logic devices based on p-/n-type modulation and their working modes. (a) Schematic diagrams of n- and p-type metal-oxide-semiconductor field-effect transistors (MOSFET). (b) Typical transfer characteristics of p- and n-type FET. Reproduced with permission from Ref. [199], © The Author(s), under exclusive licence to Springer Nature Limited 2020. (c) Relationship between carrier mobility and on/off ratio for the doped TMDC FETs. The colors represent different materials, and the shapes are the p-/n-type modulation strategies, including intrinsic defect tailoring (square), substitutional doping (circle), surface charge transfer (upper triangle), chemical intercalation (lower triangle), and electrostatic modulation (diamond). The filled and open symbols denote the electron (n-type) and hole (p-type) mobilities, respectively. The symbols covered in light color are the electron and hole mobilities of the same material. The data are from refs. [54, 67, 69, 70, 72, 94, 100, 117, 126, 134, 137, 140, 147, 148, 156, 170, 171, 175, 181, 182, 186, 196, 220]. (d) Schematic diagrams of a CMOS inverter. (e) Typical voltage transfer characteristic and the corresponding voltage gain of an inverter as a function of the input voltage. Reproduced with permission from Ref. [221], © Wiley-VCH Verlag GmbH & Co. KGaA 2020. (f) Circuit diagram of a logic NAND. (g) The typical input–output logic functions of NAND, NOR, and XOR. Reproduced with permission from Ref. [175], © American Chemical Society 2018. (h) Circuit diagram of a reconfigurable logic device. Reproduced with permission from Ref. [173], © The Author(s), under exclusive licence to Springer Nature Limited 2020. (i) Truth table of the corresponding reconfigurable logic functions in (h). Reproduced with permission from Ref. [173], © The Author(s), under exclusive licence to Springer Nature Limited 2020. The p- and n-type TMDCs in (a), (d), (f), and (h) are filled with orange and green, respectively, and the doping levels are presented by the depth of filling colors.

instance, photodetectors and LEDs [222, 223]. According to the difference in photoelectric conversion mechanism, TMDC-based photodetectors consist of photoconductors, photodiodes, and phototransistors, of which general device structures and channel doping levels are shown in Figs. 14(a) and 14(d) [224]. The main function of doping TMDCs is to modulate the energy band structures of photodiodes to optimize their carrier separation [73, 130]. For example, through the patterned intrinsic defect tailoring (n-type) and surface charge transfer (p-type) doping, a WSe_2 p-i-n photodiode was fabricated with the energy band as shown in Fig. 14(b) [70]. Beneficial from the large depleted (intrinsic region) area to effectively separate the photo-induced excitons and reduce their recombinations, the photodiode exhibits a ultrafast response speed with 3 dB bandwidth of 1.9 MHz and high specific detectivity of 10^{13} Jones, which is comparable to the commercial bulk material photodetectors (Fig. 14(c)). However, the responsivities of photodiodes are still not high because of their naturally low external quantum efficiency (EQE) [170, 225]. To enhance the photoresponsivity and balance the response speed in the same time, a n-p-n bipolar phototransistor (Fig. 14(d)) was prepared by ferroelectric-induced electrostatic modulation [212]. When illuminating light and applying positive bias voltage ($V_{CE} > 0$) on the device, the photo-induced holes in the base-collector junction drifted to the base region, and then lowered its energy band, resulting in more electrons transporting to the collector region with a photocurrent gain of 1,000 (Fig. 14(e)). Therefore, the responsivity of this phototransistor is as high as 12 $A \cdot W^{-1}$, together with a fast response time of 20 μs. In order to compare the performances of the photodetectors based on doped TMDCs, the relationship between responsivity and response time for the doped TMDC photodetectors was summed up and presented in Fig. 14(f). As can be seen, the performances of photoconductors and photodiodes are clearly separated. Photoconductors generally exhibit high responsivities with low response speeds, while photodiodes show opposite performance trends. Significantly, the doped MoS_2 n-p-n bipolar phototransistor depicts an excellent balance and proves the practicality of TMDC doping.

As another kind of photoelectric conversion device, LEDs play an important role in the applications of illumination, display, optical communication, etc. [223, 226]. When electron-hole pairs are annihilated via radiative recombination, energies that are equal to the bandgap would be deprived with photon emissions (Fig. 14(g)). Several research have been reported for the monolayer TMDC-based LEDs that are fabricated by p-/n-type modulation [169,170, 172, 223]. Figure 14(h) is an example of the electroluminescence for the WSe_2 p-n junction modulated by local gates [170]. The electroluminescence emission spectra displayed clearly gaussian peaks (1.547 eV) at

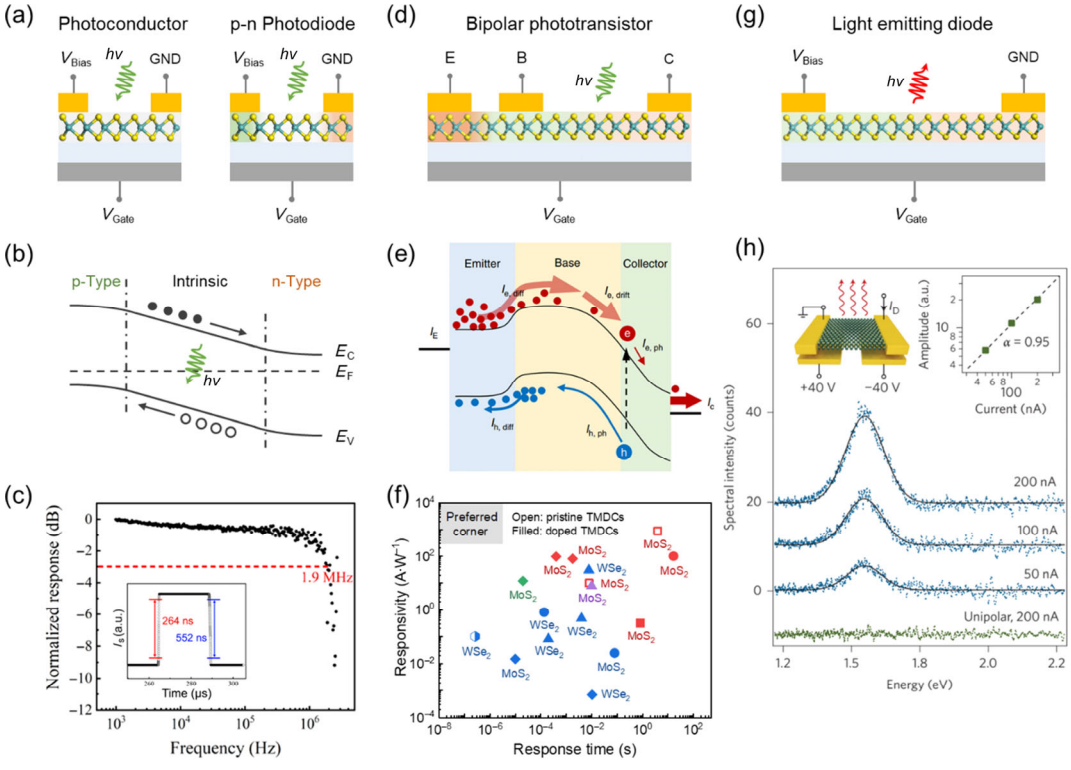

Figure 14 Photodetectors and LEDs based on p-/n-type modulation and their working modes. (a) Schematic diagrams of a photoconductor and p-n photodiode. (b) Energy band diagram of p-n photodiode under illumination. (c) Frequency response of the WSe_2 p-i-n photodiode doped by intrinsic defect tailoring (n-type) and substitutional doping (p-type). Inset: time-resolved photoresponse curve of the corresponding photodiode shows the fast rise and fall time. Reproduced with permission from Ref. [70], © American Chemical Society 2021. (d) Schematic diagrams of a bipolar phototransistor. (e) Energy band diagram of the bipolar phototransistor doped by non-volatile electrostatic modulation under illumination. Reproduced with permission from Ref. [212], © The Author(s) 2019. (f) Relationship between responsivity and response time for the doped TMDC photodetectors, including photoconductor (red), photodiode (blue), bipolar phototransistor (green), and other type of phototransistor (light purple). Symbol shapes represent different p-/n-type modulation strategies, consisting of intrinsic defect tailoring (square), substitutional doping (circle), surface charge transfer (triangle), and electrostatic modulation (diamond). The half-filled hexagon is a photodiode doped both by intrinsic defect tailoring and surface charge transfer. The filled and open symbols denote the doped and pristine TMDCs, respectively. The data are from refs. [70, 74, 91, 109, 127, 144, 150, 151, 171, 198, 212, 227–230]. (g) Schematic diagram of a LED based on p-n junction. (h) Electroluminescence emission spectra of a WSe_2 p-n junction diode with electrostatic modulation (blue and green symbols, measurements; black lines, gaussian fits). The green curve represents no light emission without electrostatic modulation. Right inset: light emission amplitude as a function of current on a double-logarithmic scale. Reproduced with permission from Ref. [170], © Macmillan Publishers Limited 2014. The p- and n-type TMDCs in (a), (d), and (g) are filled with orange and green, respectively, and the doping levels are presented by the depth of filling colors.

different currents compared with that of the unipolar device, and the light emission amplitude exhibited a linear current dependence on a double-logarithmic scale, which further verified the true light-emitting mode ambipolar carrier injection.

4 Conclusion and outlook

In recent years, the studies of TMDC-based devices have sprung up, while the doping research of TMDCs is still at the initial stage. However, there is still a lack of in-depth research in the stability of doping state, controllability of doping level, universality of doping strategy, and compatibility of doping process. In this context, we focus on the p-/n-type modulation of TMDCs and sum up the recent progress of various doping strategies consisting of intrinsic defect tailoring, substitutional doping, surface charge transfer, chemical intercalation, electrostatic modulation, and dielectric interface engineering. For each doping strategy, this review analyzes its doping mechanism and compares its advantages and disadvantages followed by the applications of semiconductor devices. In the light of these analyses, it is imperative to develop more effective methods to suppress the unintended material defects and surface adsorption, as well as to improve the metal-semiconductor contact and interface quality induced by the extremely thin thickness of TMDCs.

We are confident that in the future studies, doping will deliver more extensive applications for TMDCs in the field of novel microelectronics. Taking advantage of flexibility in doping strategies, TMDCs demonstrate a great possibility to make breakthroughs in the areas of multifunctional logic devices, ultrahigh-density data storage, multiple information photodetection, and neural network machine learning. These promising breakthroughs will give powerful support for TMDCs on the development of van der Waals integration and novel hardware architectures in the future.

Acknowledgements

This work was financially supported by the National Science Foundation of China (Nos. 61922005 and U1930105), the Beijing Municipal Natural Science Foundation (No. JQ20027), and the Fundamental Research Funds for the Central Universities (No. 048000546320504).

Conflict of interest

The authors declare no conflict of interest.

References

[1] Liu, C. S.; Chen, H. W.; Wang, S. Y.; Liu, Q.; Jiang, Y. G.; Zhang, D. W.; Liu, M.; Zhou, P. Two-dimensional materials for next-generation computing technologies. *Nat. Nanotechnol.* **2020**, *15*, 545–557.

[2] Yin, X. G.; Zhang, Y. K.; Zhu, H. L.; Wang, G. L.; Li, J. J.; Du, A. Y.; Li, C.; Zhao, L. H.; Huang, W. X.; Yang, H. et al. Vertical sandwich gate-all-around field-effect transistors with self-aligned high-k metal gates and small effective-gate-length variation. *IEEE Electron Device Lett.* **2020**, *41*, 8–11.

[3] Zhang, Z. H.; Xu, G. B.; Zhang, Q. Z.; Hou, Z. Z.; Li, J. J.; Kong, Z. Z.; Zhang, Y. K.; Xiang, J. J.; Xu, Q. X.; Wu, Z. H. et al. FinFET with improved subthreshold swing and drain current using 3-nm ferroelectric $Hf_{0.5}Zr_{0.5}O_2$. *IEEE Electron Device Lett.* **2019**, *40*, 367–370.

[4] Ionescu, A. M.; Riel, H. Tunnel field-effect transistors as energy-efficient electronic switches. *Nature* **2011**, *479*, 329–337.

[5] Hills, G.; Lau, C.; Wright, A.; Fuller, S.; Bishop, M. D.; Srimani, T.; Kanhaiya, P.; Ho, R.; Amer, A.; Stein, Y. et al. Modern microprocessor built from complementary carbon nanotube transistors. *Nature* **2019**, *572*, 595–602.

[6] Son, Y.; Frost, B.; Zhao, Y. K.; Peterson, R. L. Monolithic integration of high-voltage thin-film electronics on low-voltage integrated circuits using a solution process. *Nat. Electron.* **2019**, *2*, 540–548.

[7] Jeong, J. W.; Choi, Y. E.; Kim, W. S.; Park, J. H.; Kim, S.; Shin, S.; Lee, K.; Chang, J.; Kim, S. J.; Kim, K. R. Tunnelling-based ternary metal-oxide-semiconductor technology. *Nat. Electron.* **2019**, *2*, 307–312.

[8] Liu, Y.; Huang, Y.; Duan, X. F. Van der Waals integration before and beyond two-dimensional materials. *Nature* **2019**, *567*, 323–333.

[9] Zhu, X. J.; Li, D.; Liang, X. G.; Lu, W. D. Ionic modulation and ionic coupling effects in MoS_2 devices for neuromorphic computing. *Nat. Mater.* **2019**, *18*, 141–148.

[10] Shi, Y. Y.; Liang, X. H.; Yuan, B.; Chen, V.; Li, H. T.; Hui, F.; Yu, Z. C. W.; Yuan, F.; Pop, E.; Wong, H. S. P. et al. Electronic synapses made of layered two-dimensional materials. *Nat. Electron.* **2018**, *1*, 458–465.

[11] Jing, X.; Illarionov, Y.; Yalon, E.; Zhou, P.; Grasser, T.; Shi, Y. Y.; Lanza, M. Engineering field effect transistors with 2D semiconducting channels: Status and prospects. *Adv. Funct. Mater.* **2020**, *30*, 1901971.

[12] Akinwande, D.; Huyghebaert, C.; Wang, C. H.; Serna, M. I.; Goossens, S.; Li, L. J.; Wong, H. S. P.; Koppens, F. H. L. Graphene and two-dimensional materials for silicon technology. *Nature* **2019**, *573*, 507–518.

[13] Lin, Z. Y.; Huang, Y.; Duan, X. F. Van der Waals thin-film electronics. *Nat. Electron.* **2019**, *2*, 378–388.

[14] Liu, Y.; Duan, X. D.; Huang, Y.; Duan, X. F. Two-dimensional transistors beyond graphene and TMDCs. *Chem. Soc. Rev.* **2018**, *47*, 6388–6409.

[15] Liu, Y.; Guo, J.; Zhu, E. B.; Liao, L.; Lee, S. J.; Ding, M. N.; Shakir, I.; Gambin, V.; Huang, Y.; Duan, X. F. Approaching the Schottky-Mott limit in van der Waals metal-semiconductor junctions. *Nature* **2018**, *557*, 696–700.

[16] Wang, C.; He, Q. Y.; Halim, U.; Liu, Y. Y.; Zhu, E. B.; Lin, Z. Y.; Xiao, H.; Duan, X. D.; Feng, Z. Y.; Cheng, R. et al. Monolayer atomic crystal molecular superlattices. *Nature* **2018**, *555*, 231–236.

[17] Manzeli, S.; Ovchinnikov, D.; Pasquier, D.; Yazyev, O. V.; Kis, A. 2D transition metal dichalcogenides. *Nat. Rev. Mater.* **2017**, *2*, 17033.

[18] Song, S.; Sim, Y.; Kim, S. Y.; Kim, J. H.; Oh, I.; Na, W.; Lee, D. H.; Wang, J.; Yan, S. L.; Liu, Y. N. et al. Wafer-scale production of patterned transition metal ditelluride layers for two-dimensional metal–semiconductor contacts at the Schottky–Mott limit. *Nat. Electron.* **2020**, *3*, 207–215.

[19] He, Q. Y.; Li, P. J.; Wu, Z. H.; Yuan, B.; Luo, Z. T.; Yang, W. L.; Liu, J.; Cao, G. Q.; Zhang, W. F.; Shen, Y. L. et al. Molecular beam epitaxy scalable growth of wafer-scale continuous semiconducting monolayer $MoTe_2$ on inert amorphous dielectrics. *Adv. Mater.* **2019**, *31*, 1901578.

[20] Yang, P. F.; Zou, X. L.; Zhang, Z. P.; Hong, M.; Shi, J. P.; Chen, S. L.; Shu, J. P.; Zhao, L. Y.; Jiang, S. L.; Zhou, X. B. et al. Batch production of 6-inch uniform monolayer molybdenum disulfide catalyzed by sodium in glass. *Nat. Commun.* **2018**, *9*, 979.

[21] Shim, J.; Bae, S. H.; Kong, W.; Lee, D.; Qiao, K.; Nezich, D.; Park, Y. J.; Zhao, R. K.; Sundaram, S.; Li, X. et al. Controlled crack propagation for atomic precision handling of wafer-scale two-dimensional materials. *Science* **2018**, *362*, 665–670.

[22] Kang, K.; Lee, K. H.; Han, Y. M.; Gao, H.; Xie, S. E.; Muller, D. A.; Park, J. Layer-by-layer assembly of two-dimensional materials into wafer-scale heterostructures. *Nature* **2017**, *550*, 229–233.

[23] Kang, K.; Xie, S. E.; Huang, L. J.; Han, Y. M.; Huang, P. Y.; Mak, K. F.; Kim, C. J.; Muller, D.; Park, J. High-mobility three-atom-thick semiconducting films with wafer-scale homogeneity. *Nature* **2015**, *520*, 656–660.

[24] Sangwan, V. K.; Beck, M. E.; Henning, A.; Luo, J. J.; Bergeron, H.; Kang, J. M.; Balla, I.; Inbar, H.; Lauhon, L. J.; Hersam, M. C. Self-aligned van der Waals heterojunction diodes and transistors. *Nano Lett.* **2018**, *18*, 1421–1427.

[25] Chen, M. L.; Sun, X. D.; Liu, H.; Wang, H. W.; Zhu, Q. B.; Wang, S. S.; Du, H. F.; Dong, B. J.; Zhang, J.; Sun, Y. et al. A FinFET with

one atomic layer channel. *Nat. Commun.* **2020**, *11*, 1205.
[26] Goossens, S.; Navickaite, G.; Monasterio, C.; Gupta, S.; Piqueras, J. J.; Pérez, R.; Burwell, G.; Nikitskiy, I.; Lasanta, T.; Galán, T. et al. Broadband image sensor array based on graphene-CMOS integration. *Nat. Photonics* **2017**, *11*, 366–371.
[27] Mennel, L.; Symonowicz, J.; Wachter, S.; Polyushkin, D. K.; Molina-Mendoza, A. J.; Mueller, T. Ultrafast machine vision with 2D material neural network image sensors. *Nature* **2020**, *579*, 62–66.
[28] Chai, Y. In-sensor computing for machine vision. *Nature* **2020**, *579*, 32–33.
[29] Wang, G. C.; Li, L.; Fan, W. H.; Wang, R. Y.; Zhou, S. S.; Lü, J. T.; Gan, L.; Zhai, T. Y. Interlayer coupling induced infrared response in WS_2/MoS_2 heterostructures enhanced by surface plasmon resonance. *Adv. Funct. Mater.* **2018**, *28*, 1800339.
[30] Massicotte, M.; Vialla, F.; Schmidt, P.; Lundeberg, M. B.; Latini, S.; Haastrup, S.; Danovich, M.; Davydovskaya, D.; Watanabe, K.; Taniguchi, T. et al. Dissociation of two-dimensional excitons in monolayer WSe_2. *Nat. Commun.* **2018**, *9*, 1633.
[31] Paik, E. Y.; Zhang, L.; Burg, G. W.; Gogna, R.; Tutuc, E.; Deng, H. Interlayer exciton laser of extended spatial coherence in atomically thin heterostructures. *Nature* **2019**, *576*, 80–84.
[32] Zhao, Y. D.; Xu, K.; Pan, F.; Zhou, C. J.; Zhou, F. C.; Chai, Y. Doping, contact and interface engineering of two-dimensional layered transition metal dichalcogenides transistors. *Adv. Funct. Mater.* **2017**, *27*, 1603484.
[33] Ma, Y.; Ajayan, P. M.; Yang, S. B.; Gong, Y. J. Recent advances in synthesis and applications of 2D junctions. *Small* **2018**, *14*, 1801606.
[34] Frisenda, R.; Molina-Mendoza, A. J.; Mueller, T.; Castellanos-Gomez, A.; van der Zant, H. S. J. Atomically thin p-n junctions based on two-dimensional materials. *Chem. Soc. Rev.* **2018**, *47*, 3339–3358.
[35] Tung, R. T. The physics and chemistry of the Schottky barrier height. *Appl. Phys. Rev.* **2014**, *1*, 011304.
[36] Luo, P.; Zhuge, F. W.; Zhang, Q. F.; Chen, Y. Q.; Lv, L.; Huang, Y.; Li, H. Q.; Zhai, T. Y. Doping engineering and functionalization of two-dimensional metal chalcogenides. *Nanoscale Horiz.* **2019**, *4*, 26–51.
[37] Ugeda, M. M.; Bradley, A. J.; Shi, S. F.; da Jornada, F. H.; Zhang, Y.; Qiu, D. Y.; Ruan, W.; Mo, S. K.; Hussain, Z.; Shen, Z. X. et al. Giant bandgap renormalization and excitonic effects in a monolayer transition metal dichalcogenide semiconductor. *Nat. Mater.* **2014**, *13*, 1091–1095.
[38] Qiu, H.; Xu, T.; Wang, Z. L.; Ren, W.; Nan, H. Y.; Ni, Z. H.; Chen, Q.; Yuan, S. J.; Miao, F.; Song, F. Q. et al. Hopping transport through defect-induced localized states in molybdenum disulphide. *Nat. Commun.* **2013**, *4*, 2642.
[39] Sim, D. M.; Kim, M.; Yim, S.; Choi, M. J.; Choi, J.; Yoo, S.; Jung, Y. S. Controlled doping of vacancy-containing few-layer MoS_2 via highly stable thiol-based molecular chemisorption. *ACS Nano* **2015**, *9*, 12115–12123.
[40] Singh, A.; Singh, A. K. Origin of n-type conductivity of monolayer MoS_2. *Phys. Rev. B* **2019**, *99*, 121201(R).
[41] Tongay, S.; Zhou, J.; Ataca, C.; Liu, J.; Kang, J. S.; Matthews, T. S.; You, L.; Li, J. B.; Grossman, J. C.; Wu, J. Q. Broad-range modulation of light emission in two-dimensional semiconductors by molecular physisorption gating. *Nano Lett.* **2013**, *13*, 2831–2836.
[42] Park, K.; Kang, H.; Koo, S.; Lee, D. E.; Ryu, S. Redox-governed charge doping dictated by interfacial diffusion in two-dimensional materials. *Nat. Commun.* **2019**, *10*, 4931.
[43] Park, S.; Schultz, T.; Xu, X. M.; Wegner, B.; Aljarb, A.; Han, A. L.; Li, L. J.; Tung, V. C.; Amsalem, P.; Koch, N. Demonstration of the key substrate-dependent charge transfer mechanisms between monolayer MoS_2 and molecular dopants. *Commun. Phys.* **2019**, *2*, 109.
[44] Kong, L. G.; Zhang, X. D.; Tao, Q. Y.; Zhang, M. L.; Dang, W. Q.; Li, Z. W.; Feng, L. P.; Liao, L.; Duan, X. F.; Liu, Y. Doping-free complementary WSe_2 circuit via van der Waals metal integration. *Nat. Commun.* **2020**, *11*, 1866.
[45] Kim, C.; Moon, I.; Lee, D.; Choi, M. S.; Ahmed, F.; Nam, S.; Cho, Y.; Shin, H. J.; Park, S.; Yoo, W. J. Fermi level pinning at electrical metal contacts of monolayer molybdenum dichalcogenides. *ACS Nano* **2017**, *11*, 1588–1596.
[46] Liu, Y. Y.; Stradins, P.; Wei, S. H. Van der Waals metal-semiconductor junction: Weak Fermi level pinning enables effective tuning of Schottky barrier. *Sci. Adv.* **2016**, *2*, 1600069.
[47] Kaushik, N.; Nipane, A.; Basheer, F.; Dubey, S.; Grover, S.; Deshmukh, M. M.; Lodha, S. Schottky barrier heights for Au and Pd contacts to MoS_2. *Appl. Phys. Lett.* **2014**, *105*, 113505.
[48] Gong, C.; Colombo, L.; Wallace, R. M.; Cho, K. The unusual mechanism of partial Fermi level pinning at metal-MoS_2 interfaces. *Nano Lett.* **2014**, *14*, 1714–1720.
[49] Das, S.; Chen, H. Y.; Penumatcha, A. V.; Appenzeller, J. High performance multilayer MoS_2 transistors with scandium contacts. *Nano Lett.* **2013**, *13*, 100–105.
[50] Ma, J.; Yu, Z. G.; Zhang, Y. W. Tuning deep dopants to shallow ones in 2D semiconductors by substrate screening: The case of X_S (X = Cl, Br, I) in MoS_2. *Phys. Rev. B* **2017**, *95*, 165447.
[51] Guo, Y.; Wei, X. L.; Shu, J. P.; Liu, B.; Yin, J. B.; Guan, C. R.; Han, Y. X.; Gao, S.; Chen, Q. Charge trapping at the MoS_2-SiO_2 interface and its effects on the characteristics of MoS_2 metal-oxide-semiconductor field effect transistors. *Appl. Phys. Lett.* **2015**, *106*, 103109.
[52] Ghatak, S.; Pal, A. N.; Ghosh, A. Nature of electronic states in atomically thin MoS_2 field-effect transistors. *ACS Nano* **2011**, *5*, 7707–7712.
[53] Chen, Y.; Huang, S. X.; Ji, X.; Adepalli, K.; Yin, K. D.; Ling, X.; Wang, X. W.; Xue, J. M.; Dresselhaus, M.; Kong, J. et al. Tuning electronic structure of single layer MoS_2 through defect and interface engineering. *ACS Nano* **2018**, *12*, 2569–2579.
[54] Seo, S. Y.; Park, J.; Park, J.; Song, K.; Cha, S.; Sim, S.; Choi, S. Y.; Yeom, H. W.; Choi, H.; Jo, M. H. Writing monolithic integrated circuits on a two-dimensional semiconductor with a scanning light probe. *Nat. Electron.* **2018**, *1*, 512–517.
[55] Schmidt, H.; Giustiniano, F.; Eda, G. Electronic transport properties of transition metal dichalcogenide field-effect devices: Surface and interface effects. *Chem. Soc. Rev.* **2015**, *44*, 7715–7736.
[56] Dolui, K.; Rungger, I.; Das Pemmaraju, C.; Sanvito, S. Possible doping strategies for MoS_2 monolayers: An *ab initio* study. *Phys. Rev. B* **2013**, *88*, 075420.
[57] Zhang, Z. Z.; Wang, Z. W.; Shi, T.; Bi, C.; Rao, F.; Cai, Y. M.; Liu, Q.; Wu, H. Q.; Zhou, P. Memory materials and devices: From concept to application. *InfoMat* **2020**, *2*, 261–290.
[58] Zhu, W. J.; Low, T.; Wang, H.; Ye, P. D.; Duan, X. F. Nanoscale electronic devices based on transition metal dichalcogenides. *2D Mater.* **2019**, *6*, 032004.
[59] Ren, Y.; Yang, X. Y.; Zhou, L.; Mao, J. Y.; Han, S. T.; Zhou, Y. Recent advances in ambipolar transistors for functional applications. *Adv. Funct. Mater.* **2019**, *29*, 1902105.
[60] Ci, P. H.; Tian, X. Z.; Kang, J.; Salazar, A.; Eriguchi, K.; Warkander, S.; Tang, K. C.; Liu, J. M.; Chen, Y. B.; Tongay, S. et al. Chemical trends of deep levels in van der Waals semiconductors. *Nat. Commun.* **2020**, *11*, 5373.
[61] Oyedele, A. D.; Yang, S. Z.; Feng, T. L.; Haglund, A. V.; Gu, Y. Y.; Puretzky, A. A.; Briggs, D.; Rouleau, C. M.; Chisholm, M. F.; Unocic, R. R. et al. Defect-mediated phase transformation in anisotropic two-dimensional $PdSe_2$ crystals for seamless electrical contacts. *J. Am. Chem. Soc.* **2019**, *141*, 8928–8936.
[62] Zhu, J. Q.; Wang, Z. C.; Yu, H.; Li, N.; Zhang, J.; Meng, J. L.; Liao, M. Z.; Zhao, J.; Lu, X. B.; Du, L. J. et al. Argon Plasma induced phase transition in monolayer MoS_2. *J. Am. Chem. Soc.* **2017**, *139*, 10216–10219.
[63] McDonnell, S.; Addou, R.; Buie, C.; Wallace, R. M.; Hinkle, C. L. Defect-dominated doping and contact resistance in MoS_2. *ACS Nano* **2014**, *8*, 2880–2888.
[64] Carozo, V.; Wang, Y. X.; Fujisawa, K.; Carvalho, B. R.; McCreary, A.; Feng, S. M.; Lin, Z.; Zhou, C. J.; Perea-López, N.; Elias, A. L. et al. Optical identification of sulfur vacancies: Bound excitons at the edges of monolayer tungsten disulfide. *Sci. Adv.* **2017**, *3*, e1602813.
[65] Lin, Y. C.; Björkman, T.; Komsa, H. P.; Teng, P. Y.; Yeh, C. H.; Huang, F. S.; Lin, K. H.; Jadczak, J.; Huang, Y. S.; Chiu, P. W. et al. Three-fold rotational defects in two-dimensional transition metal dichalcogenides. *Nat. Commun.* **2015**, *6*, 6736.
[66] Gao, L.; Liao, Q. L.; Zhang, X. K.; Liu, X. Z.; Gu, L.; Liu, B. S.; Du, J. L.; Ou, Y.; Xiao, J. K.; Kang, Z. et al. Defect-engineered atomically thin MoS_2 homogeneous electronics for logic inverters. *Adv. Mater.* **2020**, *32*, 1906646.

[67] Xu, H.; Zhang, H. M.; Liu, Y. W.; Zhang, S. M.; Sun, Y. Y.; Guo, Z. X.; Sheng, Y. C.; Wang, X. D.; Luo, C.; Wu, X. et al. Controlled doping of wafer-scale $PtSe_2$ films for device application. *Adv. Funct. Mater.* **2019**, *29*, 1805614.

[68] Lin, C. P.; Chen, P. C.; Huang, J. H.; Lin, C. T.; Wang, D.; Lin, W. T.; Cheng, C. C.; Su, C. J.; Lan, Y. W.; Hou, T. H. Local modulation of electrical transport in 2D layered materials induced by electron beam irradiation. *ACS Appl. Electron. Mater.* **2019**, *1*, 684–691.

[69] Mahjouri-Samani, M.; Liang, L. B.; Oyedele, A.; Kim, Y. S.; Tian, M. K.; Cross, N.; Wang, K.; Lin, M. W.; Boulesbaa, A.; Rouleau, C. M. et al. Tailoring vacancies far beyond intrinsic levels changes the carrier type and optical response in monolayer $MoSe_{2-x}$ crystals. *Nano Lett.* **2016**, *16*, 5213–5220.

[70] Zhang, Y. W.; Ma, K. K.; Zhao, C.; Hong, W.; Nie, C. J.; Qiu, Z. J.; Wang, S. An ultrafast WSe_2 photodiode based on a lateral p-i-n homojunction. *ACS Nano* **2021**, *15*, 4405–4415.

[71] Komsa, H. P.; Kotakoski, J.; Kurasch, S.; Lehtinen, O.; Kaiser, U.; Krasheninnikov, A. V. Two-dimensional transition metal dichalcogenides under electron irradiation: Defect production and doping. *Phys. Rev. Lett.* **2012**, *109*, 035503.

[72] Seo, S. Y.; Moon, G.; Okello, O. F. N.; Park, M. Y.; Han, C.; Cha, S.; Choi, H.; Yeom, H. W.; Choi, S. Y.; Park, J. et al. Reconfigurable photo-induced doping of two-dimensional van der Waals semiconductors using different photon energies. *Nat. Electron.* **2021**, *4*, 38–44.

[73] Zhang, X. K.; Liu, B. S.; Gao, L.; Yu, H. H.; Liu, X. Z.; Du, J. L.; Xiao, J. K.; Liu, Y. H.; Gu, L.; Liao, Q. L. et al. Near-ideal van der Waals rectifiers based on all-two-dimensional Schottky junctions. *Nat. Commun.* **2021**, *12*, 1522.

[74] Zhang, X. K.; Liao, Q. L.; Liu, S.; Kang, Z.; Zhang, Z.; Du, J. L.; Li, F.; Zhang, S. H.; Xiao, J. K.; Liu, B. S. et al. Poly(4-styrenesulfonate)-induced sulfur vacancy self-healing strategy for monolayer MoS_2 homojunction photodiode. *Nat. Commun.* **2017**, *8*, 15881.

[75] Hong, J. H.; Hu, Z. X.; Probert, M.; Li, K.; Lv, D. H.; Yang, X. A.; Gu, L.; Mao, N. N.; Feng, Q. L.; Xie, L. M. et al. Exploring atomic defects in molybdenum disulphide monolayers. *Nat. Commun.* **2015**, *6*, 6293.

[76] Chee, S. S.; Lee, W. J.; Jo, Y. R.; Cho, M. K.; Chun, D. W.; Baik, H.; Kim, B. J.; Yoon, M. H.; Lee, K.; Ham, M. H. Atomic vacancy control and elemental substitution in a monolayer molybdenum disulfide for high performance optoelectronic device arrays. *Adv. Funct. Mater.* **2020**, *30*, 1908147.

[77] Komsa, H. P.; Krasheninnikov, A. V. Native defects in bulk and monolayer MoS_2 from first principles. *Phys. Rev. B* **2015**, *91*, 125304.

[78] Shang, M. H.; Hou, H. L.; Zheng, J. J.; Yang, Z. B.; Zhang, J.; Wei, S. H.; Duan, X. M.; Yang, W. Y. Elimination of S vacancy as the cause for the n-type behavior of MoS_2 from the first-principles perspective. *J. Phys. Chem. Lett.* **2018**, *9*, 6032–6037.

[79] Onofrio, N.; Guzman, D.; Strachan, A. Novel doping alternatives for single-layer transition metal dichalcogenides. *J. Appl. Phys.* **2017**, *122*, 185102.

[80] Lin, Y. C.; Torsi, R.; Geohegan, D. B.; Robinson, J. A.; Xiao, K. Controllable thin-film approaches for doping and alloying transition metal dichalcogenides monolayers. *Adv. Sci.*, in press, DOI: 10.1002/advs.202004249.

[81] Loh, L.; Zhang, Z. P.; Bosman, M.; Eda, G. Substitutional doping in 2D transition metal dichalcogenides. *Nano Res.* **2021**, *14*, 1668–1681.

[82] Samadi, M.; Sarikhani, N.; Zirak, M.; Zhang, H.; Zhang, H. L.; Moshfegh, A. Z. Group 6 transition metal dichalcogenide nanomaterials: Synthesis, applications and future perspectives. *Nanoscale Horiz.* **2018**, *3*, 90–204.

[83] Suh, J.; Park, T. E.; Lin, D. Y.; Fu, D. Y.; Park, J.; Jung, H. J.; Chen, Y. B.; Ko, C.; Jang, C.; Sun, Y. H. et al. Doping against the native propensity of MoS_2: Degenerate hole doping by cation substitution. *Nano Lett.* **2014**, *14*, 6976–6982.

[84] Laskar, M. R.; Nath, D. N.; Ma, L.; Lee II, E. W.; Lee, C. H.; Kent, T.; Yang, Z. H.; Mishra, R.; Roldan, M. A.; Idrobo, J. C. et al. p-type doping of MoS_2 thin films using Nb. *Appl. Phys. Lett.* **2014**, *104*, 092104.

[85] Li, M. G.; Yao, J. D.; Wu, X. X.; Zhang, S. C.; Xing, B. R.; Niu, X. Y.; Yan, X. Y.; Yu, Y.; Liu, Y. L.; Wang, Y. W. P-type doping in large-area monolayer MoS_2 by chemical vapor deposition. *ACS Appl. Mater. Interfaces* **2020**, *12*, 6276–6282.

[86] Gao, J.; Kim, Y. D.; Liang, L. B.; Idrobo, J. C.; Chow, P.; Tan, J. W.; Li, B. C.; Li, L.; Sumpter, B. G.; Lu, T. M. et al. Transition-metal substitution doping in synthetic atomically thin semiconductors. *Adv. Mater.* **2016**, *28*, 9735–9743.

[87] Sasaki, S.; Kobayashi, Y.; Liu, Z.; Suenaga, K.; Maniwa, Y.; Miyauchi, Y.; Miyata, Y. Growth and optical properties of Nb-doped WS_2 monolayers. *Appl. Phys. Express* **2016**, *9*, 071201.

[88] Jin, Y. Y.; Zeng, Z. Y.; Xu, Z. W.; Lin, Y. C.; Bi, K. X.; Shao, G. L.; Hu, T. S.; Wang, S. S.; Li, S. S.; Suenaga, K. et al. Synthesis and transport properties of degenerate P-Type Nb-doped WS_2 monolayers. *Chem. Mater.* **2019**, *31*, 3534–3541.

[89] Qin, Z. Y.; Loh, L.; Wang, J. Y.; Xu, X. M.; Zhang, Q.; Haas, B.; Alvarez, C.; Okuno, H.; Yong, J. Z.; Schultz, T. et al. Growth of Nb-doped monolayer WS_2 by liquid-phase precursor mixing. *ACS Nano* **2019**, *13*, 10768–10775.

[90] Gao, H.; Suh, J.; Cao, M. C.; Joe, A. Y.; Mujid, F.; Lee, K. H.; Xie, S. E.; Poddar, P.; Lee, J. U.; Kang, K. et al. Tuning electrical conductance of MoS_2 monolayers through substitutional doping. *Nano Lett.* **2020**, *20*, 4095–4101.

[91] Svatek, S. A.; Antolin, E.; Lin, D. Y.; Frisenda, R.; Reuter, C.; Molina-Mendoza, A. J.; Muñoz, M.; Agraït, N.; Ko, T. S.; de Lara, D. P. et al. Gate tunable photovoltaic effect in MoS_2 vertical p-n homostructures. *J. Mater. Chem. C* **2017**, *5*, 854–861.

[92] Zhang, L. L.; Wang, G.; Zhang, Y. B.; Cao, Z. P.; Wang, Y.; Cao, T. J.; Wang, C.; Cheng, B.; Zhang, W. Q.; Wan, X. G. et al. Tuning electrical conductance in bilayer MoS_2 through defect-mediated interlayer chemical bonding. *ACS Nano* **2020**, *14*, 10265–10275.

[93] Zhang, T. Y.; Fujisawa, K.; Zhang, F.; Liu, M. Z.; Lucking, M. C.; Gontijo, R. N.; Lei, Y.; Liu, H.; Crust, K.; Granzier-Nakajima, T. et al. Universal *in situ* substitutional doping of transition metal dichalcogenides by liquid-phase precursor-assisted synthesis. *ACS Nano* **2020**, *14*, 4326–4335.

[94] Wu, S. X.; Zeng, Y.; Zeng, X. B.; Wang, S. B.; Hu, Y. S.; Wang, W. Z.; Yin, S.; Zhou, G. T.; Jin, W.; Ren, T. T. et al. High-performance p-type MoS_2 field-effect transistor by toroidal-magnetic-field controlled oxygen Plasma doping. *2D Mater.* **2019**, *6*, 025007.

[95] Chen, M. K.; Nam, H.; Wi, S.; Ji, L.; Ren, X.; Bian, L. F.; Lu, S. L.; Liang, X. G. Stable few-layer MoS_2 rectifying diodes formed by plasma-assisted doping. *Appl. Phys. Lett.* **2013**, *103*, 142110.

[96] Qu, D. S.; Liu, X. C.; Huang, M.; Lee, C.; Ahmed, F.; Kim, H.; Ruoff, R. S.; Hone, J.; Yoo, W. J. Carrier-type modulation and mobility improvement of thin $MoTe_2$. *Adv. Mater.* **2017**, *29*, 1606433.

[97] Zhang, F.; Lu, Y. F.; Schulman, D. S.; Zhang, T. Y.; Fujisawa, K.; Lin, Z.; Lei, Y.; Elias, A. L.; Das, S.; Sinnott, S. B. et al. Carbon doping of WS_2 monolayers: Bandgap reduction and p-type doping transport. *Sci. Adv.* **2019**, *5*, eaav5003.

[98] Wi, S.; Kim, H.; Chen, M. K.; Nam, H.; Guo, L. J.; Meyhofer, E.; Liang, X. G. Enhancement of photovoltaic response in multilayer MoS_2 induced by Plasma doping. *ACS Nano* **2014**, *8*, 5270–5281.

[99] Cao, Q.; Dai, Y. W.; Xu, J.; Chen, L.; Zhu, H.; Sun, Q. Q.; Zhang, D. W. Realizing stable p-type transporting in two-dimensional WS_2 films. *ACS Appl. Mater. Interfaces* **2017**, *9*, 18215–18221.

[100] Tang, B. S.; Yu, Z. G.; Huang, L.; Chai, J. W.; Wong, S. L.; Deng, J.; Yang, W. F.; Gong, H.; Wang, S. J.; Ang, K. W. et al. Direct n- to p-type channel conversion in monolayer/few-layer WS_2 field-effect transistors by atomic nitrogen treatment. *ACS Nano* **2018**, *12*, 2506–2513.

[101] Jiang, J. F.; Zhang, Q. H.; Wang, A. Z.; Zhang, Y.; Meng, F. Q.; Zhang, C. C.; Feng, X. J.; Feng, Y. P.; Gu, L.; Liu, H. et al. A facile and effective method for patching sulfur vacancies of WS_2 via nitrogen Plasma treatment. *Small* **2019**, *15*, 1901791.

[102] Nipane, A.; Karmakar, D.; Kaushik, N.; Karande, S.; Lodha, S. Few-layer MoS_2 p-type devices enabled by selective doping using low energy phosphorus implantation. *ACS Nano* **2016**, *10*, 2128–2137.

[103] Haynes, K.; Murray, R.; Weinrich, Z.; Zhao, X.; Chiappe, D.; Sutar, S.; Radu, I.; Hatem, C.; Perry, S. S.; Jones, K. S. Modulating the resistivity of MoS_2 through low energy phosphorus plasma implantation. *Appl. Phys. Lett.* **2017**, *110*, 262102.

[104] Kim, E.; Ko, C.; Kim, K.; Chen, Y. B.; Suh, J.; Ryu, S. G.; Wu, K. D.; Meng, X. Q.; Suslu, A.; Tongay, S. et al. Site selective doping of ultrathin metal dichalcogenides by laser-assisted reaction. *Adv. Mater.* **2016**, *28*, 341–346.

[105] Chang, R. J.; Sheng, Y. W.; Ryu, G. H.; Mkhize, N.; Chen, T. X.; Lu, Y.; Chen, J.; Lee, J. K.; Bhaskaran, H.; Warner, J. H. Postgrowth substitutional tin doping of 2D WS_2 crystals using chemical vapor deposition. *ACS Appl. Mater. Interfaces* **2019**, *11*, 24279–24288.

[106] Zhang, K. H.; Bersch, B. M.; Joshi, J.; Addou, R.; Cormier, C. R.; Zhang, C. X.; Xu, K.; Briggs, N. C.; Wang, K.; Subramanian, S. et al. Tuning the electronic and photonic properties of monolayer MoS_2 via *in situ* rhenium substitutional doping. *Adv. Funct. Mater.* **2018**, *28*, 1706950.

[107] Tian, X. Z.; Kim, D. S.; Yang, S. Z.; Ciccarino, C. J.; Gong, Y. J.; Yang, Y.; Yang, Y.; Duschatko, B.; Yuan, Y. K.; Ajayan, P. M. et al. Correlating the three-dimensional atomic defects and electronic properties of two-dimensional transition metal dichalcogenides. *Nat. Mater.* **2020**, *19*, 867–873.

[108] Cai, Z. Y.; Shen, T. Z.; Zhu, Q.; Feng, S. M.; Yu, Q. M.; Liu, J. M.; Tang, L.; Zhao, Y.; Wang, J. W.; Liu, B. L. et al. Dual-additive assisted chemical vapor deposition for the growth of Mn-Doped 2D MoS_2 with tunable electronic properties. *Small* **2020**, *16*, 1903181.

[109] Li, S. Y.; Chen, X. Q.; Liu, F. M.; Chen, Y. F.; Liu, B.; Deng, W. J.; An, B. X.; Chu, F. H.; Zhang, G. Q.; Li, S. L. et al. Enhanced performance of a CVD MoS_2 photodetector by chemical *in situ* n-type doping. *ACS Appl. Mater. Interfaces* **2019**, *11*, 11636–11644.

[110] Lin, X. Q.; Ni, J. Charge and magnetic states of Mn-, Fe-, and Co-doped monolayer MoS_2. *J. Appl. Phys.* **2014**, *116*, 044311.

[111] Wang, J. Q.; Sun, F.; Yang, S.; Li, Y. T.; Zhao, C.; Xu, M. W.; Zhang, Y.; Zeng, H. Robust ferromagnetism in Mn-doped MoS_2 nanostructures. *Appl. Phys. Lett.* **2016**, *109*, 092401.

[112] Fang, Q. L.; Zhao, X. M.; Huang, Y. H.; Xu, K. W.; Min, T.; Chu, P. K.; Ma, F. Structural stability and magnetic-exchange coupling in Mn-doped monolayer/bilayer MoS_2. *Phys. Chem. Chem. Phys.* **2018**, *20*, 553–561.

[113] Li, Q.; Zhao, X. X.; Deng, L. J.; Shi, Z. T.; Liu, S.; Wei, Q. L.; Zhang, L. B.; Lu, H. P.; Gao, W. B.; Huang, W. et al. Enhanced valley zeeman splitting in Fe-Doped monolayer MoS_2. *ACS Nano* **2020**, *14*, 4636–4645.

[114] Bai, Z. T.; Zhang, L.; Liu, L. Improving low-energy boron/nitrogen ion implantation in graphene by ion bombardment at oblique angles. *Nanoscale* **2016**, *8*, 8761–8772.

[115] Jang, C. W.; Kim, J. H.; Lee, D. H.; Shin, D. H.; Kim, S.; Choi, S. H.; Hwang, E.; Elliman, R. G. Effect of stopping-layer-assisted boron-ion implantation on the electrical properties of graphene: Interplay between strain and charge doping. *Carbon* **2017**, *118*, 343–347.

[116] Pham, V. P.; Yeom, G. Y. Recent advances in doping of molybdenum disulfide: Industrial applications and future prospects. *Adv. Mater.* **2016**, *28*, 9024–9059.

[117] Chang, Y. M.; Yang, S. H.; Lin, C. Y.; Chen, C. H.; Lien, C. H.; Jian, W. B.; Ueno, K.; Suen, Y. W.; Tsukagoshi, K.; Lin, Y. F. Reversible and precisely controllable p/n-Type doping of $MoTe_2$ transistors through electrothermal doping. *Adv. Mater.* **2018**, *30*, 1706995.

[118] Fang, H.; Chuang, S.; Chang, T. C.; Takei, K.; Takahashi, T.; Javey, A. High-performance single layered WSe_2 p-FETs with chemically doped contacts. *Nano Lett.* **2012**, *12*, 3788–3792.

[119] Liu, B. L.; Chen, L.; Liu, G.; Abbas, A. N.; Fathi, M.; Zhou, C. W. High-performance chemical sensing using Schottky-contacted chemical vapor deposition grown monolayer MoS_2 transistors. *ACS Nano* **2014**, *8*, 5304–5314.

[120] McDonnell, S.; Azcatl, A.; Addou, R.; Gong, C.; Battaglia, C.; Chuang, S.; Cho, K.; Javey, A.; Wallace, R. M. Hole contacts on transition metal dichalcogenides: Interface chemistry and band alignments. *ACS Nano* **2014**, *8*, 6265–6272.

[121] Yang, S.; Lee, G.; Kim, J. Selective p-doping of 2D WSe_2 via UV/ozone treatments and its application in field-effect transistors. *ACS Appl. Mater. Interfaces* **2021**, *13*, 955–961.

[122] Xie, Y.; Wu, E. X.; Hu, R. X.; Qian, S. B.; Feng, Z. H.; Chen, X. J.; Zhang, H.; Xu, L. Y.; Hu, X. D.; Liu, J. et al. Enhancing electronic and optoelectronic performances of tungsten diselenide by plasma treatment. *Nanoscale* **2018**, *10*, 12436–12444.

[123] Sarkar, D.; Xie, X. J.; Kang, J. H.; Zhang, H. J.; Liu, W.; Navarrete, J.; Moskovits, M.; Banerjee, K. Functionalization of transition metal dichalcogenides with metallic nanoparticles: Implications for doping and gas-sensing. *Nano Lett.* **2015**, *15*, 2852–2862.

[124] Choi, M. S.; Qu, D. S.; Lee, D.; Liu, X. C.; Watanabe, K.; Taniguchi, T.; Yoo, W. J. Lateral MoS_2 p-n junction formed by chemical doping for use in high-performance optoelectronics. *ACS Nano* **2014**, *8*, 9332–9340.

[125] Li, H. M.; Lee, D.; Qu, D. S.; Liu, X. C.; Ryu, J.; Seabaugh, A.; Yoo, W. J. Ultimate thin vertical p-n junction composed of two-dimensional layered molybdenum disulfide. *Nat. Commun.* **2015**, *6*, 6564.

[126] Liu, X. C.; Qu, D. S.; Ryu, J.; Ahmed, F.; Yang, Z.; Lee, D.; Yoo, W. J. P-type polar transition of chemically doped multilayer MoS_2 transistor. *Adv. Mater.* **2016**, *28*, 2345–2351.

[127] Huo, N. J.; Konstantatos, G. Ultrasensitive all-2D MoS_2 phototransistors enabled by an out-of-plane MoS_2 PN homojunction. *Nat. Commun.* **2017**, *8*, 572.

[128] Liu, X. C.; Qu, D. S.; Choi, M. S.; Lee, C.; Kim, H.; Yoo, W. J. Homogeneous molybdenum disulfide tunnel diode formed via chemical doping. *Appl. Phys. Lett.* **2018**, *112*, 183103.

[129] Zhang, K.; Zhai, J. Y.; Wang, Z. L. A monolayer MoS_2 p-n homogenous photodiode with enhanced photoresponse by piezo-phototronic effect. *2D Mater.* **2018**, *5*, 035038.

[130] Jang, H.; Seok, Y.; Choi, Y. T.; Cho, S. H.; Watanabe, K.; Taniguchi, T.; Lee, K. High-performance near-infrared photodetectors based on surface-doped InSe. *Adv. Funct. Mater.* **2021**, *31*, 2006788.

[131] Lei, S. D.; Wang, X. F.; Li, B.; Kang, J. H.; He, Y. M.; George, A.; Ge, L. H.; Gong, Y. J.; Dong, P.; Jin, Z. H. et al. Surface functionalization of two-dimensional metal chalcogenides by Lewis acid-base chemistry. *Nat. Nanotechnol.* **2016**, *11*, 465–471.

[132] Kim, J.; Heo, K.; Kang, D. H.; Shin, C.; Lee, S.; Yu, H. Y.; Park, J. H. Rhenium diselenide ($ReSe_2$) near-infrared photodetector: Performance enhancement by selective p-doping technique. *Adv. Sci.* **2019**, *6*, 1901255.

[133] Park, J. H.; Rai, A.; Hwang, J.; Zhang, C. X.; Kwak, I.; Wolf, S. F.; Vishwanath, S.; Liu, X. Y.; Dobrowolska, M.; Furdyna, J. et al. Band structure engineering of layered WSe_2 via one-step chemical functionalization. *ACS Nano* **2019**, *13*, 7545–7555.

[134] Ji, H. G.; Solís-Fernández, P.; Yoshimura, D.; Maruyama, M.; Endo, T.; Miyata, Y.; Okada, S.; Ago, H. Chemically tuned p- and n-type WSe_2 monolayers with high carrier mobility for advanced electronics. *Adv. Mater.* **2019**, *31*, 1903613.

[135] Mouri, S.; Miyauchi, Y.; Matsuda, K. Tunable photoluminescence of monolayer MoS_2 via chemical doping. *Nano Lett.* **2013**, *13*, 5944–5948.

[136] Kang, D. H.; Kim, M. S.; Shim, J.; Jeon, J.; Park, H. Y.; Jung, W. S.; Yu, H. Y.; Pang, C. H.; Lee, S.; Park, J. H. High-performance transition metal dichalcogenide photodetectors enhanced by self-assembled monolayer doping. *Adv. Funct. Mater.* **2015**, *25*, 4219–4227.

[137] Fang, H.; Tosun, M.; Seol, G.; Chang, T. C.; Takei, K.; Guo, J.; Javey, A. Degenerate n-doping of few-layer transition metal dichalcogenides by potassium. *Nano Lett.* **2013**, *13*, 1991–1995.

[138] Qi, D. Y.; Han, C.; Rong, X. M.; Zhang, X. W.; Chhowalla, M.; Wee, A. T. S.; Zhang, W. J. Continuously tuning electronic properties of few-layer molybdenum ditelluride with *in situ* aluminum modification toward ultrahigh gain complementary inverters. *ACS Nano* **2019**, *13*, 9464–9472.

[139] Lin, J. D.; Han, C.; Wang, F.; Wang, R.; Xiang, D.; Qin, S. Q.; Zhang, X. A.; Wang, L.; Zhang, H.; Wee, A. T. S. et al. Electron-doping-enhanced trion formation in monolayer molybdenum disulfide functionalized with cesium carbonate. *ACS Nano* **2014**, *8*, 5323–5329.

[140] Park, Y. J.; Katiyar, A. K.; Hoang, A. T.; Ahn, J. H. Controllable P- and N-type conversion of $MoTe_2$ via oxide interfacial layer for logic circuits. *Small* **2019**, *15*, 1901772.

[141] Lim, J. Y.; Pezeshki, A.; Oh, S.; Kim, J. S.; Lee, Y. T.; Yu, S.; Hwang, D. K.; Lee, G. H.; Choi, H. J.; Im, S. Homogeneous 2D

$MoTe_2$ p-n junctions and CMOS inverters formed by atomic-layer-deposition-induced doping. *Adv. Mater.* **2017**, *29*, 1701798.

[142] Hemanjaneyulu, K.; Kumar, J.; Shrivastava, M. MoS_2 doping using potassium iodide for reliable contacts and efficient FET operation. *IEEE Trans. Electron Devices* **2019**, *66*, 3224–3228.

[143] Khalil, H. M. W.; Khan, M. F.; Eom, J.; Noh, H. Highly stable and tunable chemical doping of multilayer WS_2 field effect transistor: Reduction in contact resistance. *ACS Appl. Mater. Interfaces* **2015**, *7*, 23589–23596.

[144] Yang, Y. J.; Huo, N. J.; Li, J. B. Gate-tunable and high optoelectronic performance in multilayer WSe_2 P-N diode. *J. Mater. Chem. C* **2018**, *6*, 11673–11678.

[145] Sun, M. X.; Xie, D.; Sun, Y. L.; Li, W. W.; Ren, T. L. Locally hydrazine doped WSe_2 p-n junction toward high-performance photodetectors. *Nanotechnology* **2018**, *29*, 015203.

[146] Lee, I.; Rathi, S.; Li, L. J.; Lim, D.; Khan, M. A.; Kannan, E. S.; Kim, G. H. Non-degenerate n-type doping by hydrazine treatment in metal work function engineered WSe_2 field-effect transistor. *Nanotechnology* **2015**, *26*, 455203.

[147] Kiriya, D.; Tosun, M.; Zhao, P. D.; Kang, J. S.; Javey, A. Air-stable surface charge transfer doping of MoS_2 by benzyl viologen. *J. Am. Chem. Soc.* **2014**, *136*, 7853–7856.

[148] Wan, D.; Jiang, B.; Huang, H.; Chen, C.; Abliz, A.; Ye, C.; Liu, X. Q.; Zou, X. M; Li, G. L.; Flandre, D. et al. High voltage gain WSe_2 complementary compact inverter with buried gate for local doping. *IEEE Electron Device Lett.* **2020**, *41*, 944–947.

[149] Yang, L. M.; Majumdar, K.; Liu, H.; Du, Y. C.; Wu, H.; Hatzistergos, M.; Hung, P. Y.; Tieckelmann, R.; Tsai, W.; Hobbs, C. et al. Chloride molecular doping technique on 2D materials: WS_2 and MoS_2. *Nano Lett.* **2014**, *14*, 6275–6280.

[150] Sun, J. C.; Wang, Y. Y.; Guo, S. Q.; Wan, B. S.; Dong, L. Q.; Gu, Y. D.; Song, C.; Pan, C. F.; Zhang, Q.; Gu, L. et al. Lateral 2D WSe_2 p-n homojunction formed by efficient charge-carrier-type modulation for high-performance optoelectronics. *Adv. Mater.* **2020**, *32*, 1906499.

[151] Tang, Y. C.; Wang, Z.; Wang, P.; Wu, F.; Wang, Y. M.; Chen, Y. F.; Wang, H. L.; Peng, M.; Shan, C. X.; Zhu, Z. H. et al. WSe_2 photovoltaic device based on intramolecular p-n junction. *Small* **2019**, *15*, 1805545.

[152] Du, Y. C.; Liu, H.; Neal, A. T.; Si, M. W.; Ye, P. D. Molecular doping of multilayer MoS_2 field-effect transistors: Reduction in sheet and contact resistances. *IEEE Electron Device Lett.* **2013**, *34*, 1328–1330.

[153] Arnold, A. J.; Schulman, D. S.; Das, S. Thickness trends of electron and hole conduction and contact carrier injection in surface charge transfer doped 2D field effect transistors. *ACS Nano* **2020**, *14*, 13557–13568.

[154] Shi, Y. M.; Kim, K. K.; Reina, A.; Hofmann, M.; Li, L. J.; Kong, J. Work function engineering of graphene electrode via chemical doping. *ACS Nano* **2010**, *4*, 2689–2694.

[155] Rajapakse, M.; Karki, B.; Abu, U. O.; Pishgar, S.; Musa, M. R. K.; Riyadh, S. M. S.; Yu, M.; Sumanasekera, G.; Jasinski, J. B. Intercalation as a versatile tool for fabrication, property tuning, and phase transitions in 2D materials. *npj 2D Mater. Appl.* **2021**, *5*, 30.

[156] Gong, Y. J.; Yuan, H. T.; Wu, C. L.; Tang, P. Z.; Yang, S. Z.; Yang, A. K.; Li, G. D.; Liu, B. F.; van de Groep, J.; Brongersma, M. L. et al. Spatially controlled doping of two-dimensional SnS_2 through intercalation for electronics. *Nat. Nanotechnol.* **2018**, *13*, 294–299.

[157] Kim, D. K.; Hong, S. B.; Jeong, K.; Lee, C.; Kim, H.; Cho, M. H. P-N junction diode using Plasma boron-doped black phosphorus for high-performance photovoltaic devices. *ACS Nano* **2019**, *13*, 1683–1693.

[158] Fan, X. B.; Xu, P. T.; Zhou, D. K.; Sun, Y. F.; Li, Y. C.; Nguyen, M. A. T.; Terrones, M.; Mallouk, T. E. Fast and efficient preparation of exfoliated 2H MoS_2 nanosheets by sonication-assisted lithium intercalation and infrared laser-induced 1T to 2H phase reversion. *Nano Lett.* **2015**, *15*, 5956–5960.

[159] Acerce, M.; Voiry, D.; Chhowalla, M. Metallic 1T phase MoS_2 nanosheets as supercapacitor electrode materials. *Nat. Nanotechnol.* **2015**, *10*, 313–318.

[160] Liu, C.; Lian, C. S.; Liao, M. H.; Wang, Y.; Zhong, Y.; Ding, C.; Li, W.; Song, C. L.; He, K.; Ma, X. C. et al. Two-dimensional superconductivity and topological states in $PdTe_2$ thin films. *Phys. Rev. Mater.* **2018**, *2*, 094001.

[161] Wan, J. Y.; Lacey, S. D.; Dai, J. Q.; Bao, W. Z.; Fuhrer, M. S.; Hu, L. Tuning two-dimensional nanomaterials by intercalation: Materials, properties and applications. *Chem. Soc. Rev.* **2016**, *45*, 6742–6765.

[162] Wan, C. L.; Gu, X. K.; Dang, F.; Itoh, T.; Wang, Y. F.; Sasaki, H.; Kondo, M.; Koga, K.; Yabuki, K.; Snyder, G. J. et al. Flexible n-type thermoelectric materials by organic intercalation of layered transition metal dichalcogenide TiS_2. *Nat. Mater.* **2015**, *14*, 622–627.

[163] Koski, K. J.; Wessells, C. D.; Reed, B. W.; Cha, J. J.; Kong, D. S.; Cui, Y. Chemical intercalation of zerovalent metals into 2D layered Bi_2Se_3 nanoribbons. *J. Am. Chem. Soc.* **2012**, *134*, 13773–13779.

[164] Kumar, A.; Roy, J. N. A physics-based threshold voltage model for junction-less double gate FETs having vertical structural and doping asymmetry. *IEEE Trans. Electron Devices* **2019**, *66*, 3640–3645.

[165] Liu, C. S.; Chen, H. W.; Hou, X.; Zhang, H.; Han, J.; Jiang, Y. G.; Zeng, X. Y.; Zhang, D. W.; Zhou, P. Small footprint transistor architecture for photoswitching logic and *in situ* memory. *Nat. Nanotechnol.* **2019**, *14*, 662–667.

[166] Beck, M. E.; Hersam, M. C. Emerging opportunities for electrostatic control in atomically thin devices. *ACS Nano* **2020**, *14*, 6498–6518.

[167] Gabor, N. M.; Song, J. C. W.; Ma, Q.; Nair, N. L.; Taychatanapat, T.; Watanabe, K.; Taniguchi, T.; Levitov, L. S.; Jarillo-Herrero, P. Hot carrier-assisted intrinsic photoresponse in graphene. *Science* **2011**, *334*, 648–652.

[168] Chiu, H. Y.; Perebeinos, V.; Lin, Y. M.; Avouris, P. Controllable p-n junction formation in monolayer graphene using electrostatic substrate engineering. *Nano Lett.* **2010**, *10*, 4634–4639.

[169] Ross, J. S.; Klement, P.; Jones, A. M.; Ghimire, N. J.; Yan, J. Q.; Mandrus, D. G.; Taniguchi, T.; Watanabe, K.; Kitamura, K.; Yao, W. et al. Electrically tunable excitonic light-emitting diodes based on monolayer WSe_2 p-n junctions. *Nat. Nanotechnol.* **2014**, *9*, 268–272.

[170] Pospischil, A.; Furchi, M. M.; Mueller, T. Solar-energy conversion and light emission in an atomic monolayer p-n diode. *Nat. Nanotechnol.* **2014**, *9*, 257–261.

[171] Groenendijk, D. J.; Buscema, M.; Steele, G. A.; Michaelis de Vasconcellos, S.; Bratschitsch, R.; van der Zant, H. S. J.; Castellanos-Gomez, A. Photovoltaic and photothermoelectric effect in a double-gated WSe_2 device. *Nano Lett.* **2014**, *14*, 5846–5852.

[172] Baugher, B. W. H.; Churchill, H. O. H.; Yang, Y. F.; Jarillo-Herrero, P. Optoelectronic devices based on electrically tunable p-n diodes in a monolayer dichalcogenide. *Nat. Nanotechnol.* **2014**, *9*, 262–267.

[173] Pan, C.; Wang, C. Y.; Liang, S. J.; Wang, Y.; Cao, T. J.; Wang, P. F.; Wang, C.; Wang, S.; Cheng, B.; Gao, A. Y. et al. Reconfigurable logic and neuromorphic circuits based on electrically tunable two-dimensional homojunctions. *Nat. Electron.* **2020**, *3*, 383–390.

[174] Illarionov, Y. Y.; Knobloch, T.; Jech, M.; Lanza, M.; Akinwande, D.; Vexler, M. I.; Mueller, T.; Lemme, M. C.; Fiori, G.; Schwierz, F. et al. Insulators for 2D nanoelectronics: The gap to bridge. *Nat. Commun.* **2020**, *11*, 3385.

[175] Resta, G. V.; Balaji, Y.; Lin, D.; Radu, I. P.; Catthoor, F.; Gaillardon, P. E.; De Micheli, G. Doping-free complementary logic gates enabled by two-dimensional polarity-controllable transistors. *ACS Nano* **2018**, *12*, 7039–7047.

[176] Illarionov, Y. Y.; Banshchikov, A. G.; Polyushkin, D. K.; Wachter, S.; Knobloch, T.; Thesberg, M.; Mennel, L.; Paur, M.; Stöger-Pollach, M.; Steiger-Thirsfeld, A. et al. Ultrathin calcium fluoride insulators for two-dimensional field-effect transistors. *Nat. Electron.* **2019**, *2*, 230–235.

[177] Wen, C.; Banshchikov, A. G.; Illarionov, Y. Y.; Frammelsberger, W.; Knobloch, T.; Hui, F.; Sokolov, N. S.; Grasser, T.; Lanza, M. Dielectric properties of ultrathin CaF_2 ionic crystals. *Adv. Mater.* **2020**, *32*, 2002525.

[178] Knobloch, T.; Illarionov, Y. Y.; Ducry, F.; Schleich, C.; Wachter, S.; Watanabe, K.; Taniguchi, T.; Mueller, T.; Waltl, M.; Lanza, M. et al. The performance limits of hexagonal boron nitride as an insulator

for scaled CMOS devices based on two-dimensional materials. *Nat. Electron.* **2021**, *4*, 98–108.
[179] Wang, J. I. J.; Yang, Y. F.; Chen, Y. A.; Watanabe, K.; Taniguchi, T.; Churchill, H. O. H.; Jarillo-Herrero, P. Electronic transport of encapsulated graphene and WSe_2 devices fabricated by pick-up of prepatterned hBN. *Nano Lett.* **2015**, *15*, 1898–1903.
[180] Chuang, H. J.; Tan, X. B.; Ghimire, N. J.; Perera, M. M.; Chamlagain, B.; Cheng, M. M. C.; Yan, J. Q.; Mandrus, D.; Tománek, D.; Zhou, Z. X. High mobility WSe_2 p- and n-type field-effect transistors contacted by highly doped graphene for low-resistance contacts. *Nano Lett.* **2014**, *14*, 3594–3601.
[181] Zhang, Y. J.; Ye, J. T.; Yomogida, Y.; Takenobu, T.; Iwasa, Y. Formation of a stable p-n junction in a liquid-gated MoS_2 ambipolar transistor. *Nano Lett.* **2013**, *13*, 3023–3028.
[182] Zhang, Y. J.; Ye, J. T.; Matsuhashi, Y.; Iwasa, Y. Ambipolar MoS_2 thin flake transistors. *Nano Lett.* **2012**, *12*, 1136–1140.
[183] Wu, C. L.; Yuan, H. T.; Li, Y. B.; Gong, Y. J.; Hwang, H. Y.; Cui, Y. Gate-induced metal-insulator transition in MoS_2 by solid superionic conductor LaF_3. *Nano Lett.* **2018**, *18*, 2387–2392.
[184] Meng, Y. Z.; Wang, T. M.; Jin, C. H.; Li, Z. P.; Miao, S. N.; Lian, Z.; Taniguchi, T.; Watanabe, K.; Song, F. Q.; Shi, S. F. Electrical switching between exciton dissociation to exciton funneling in $MoSe_2/WS_2$ heterostructure. *Nat. Commun.* **2020**, *11*, 2640.
[185] Li, J. F.; Chen, X. Q.; Xiao, Y.; Li, S. Y.; Zhang, G. Q.; Diao, X. G.; Yan, H.; Zhang, Y. Z. A tunable floating-base bipolar transistor based on a 2D material homojunction realized using a solid ionic dielectric material. *Nanoscale* **2019**, *11*, 22531–22538.
[186] Wu, E. X.; Xie, Y.; Zhang, J.; Zhang, H.; Hu, X. D.; Liu, J.; Zhou, C. W.; Zhang, D. H. Dynamically controllable polarity modulation of $MoTe_2$ field-effect transistors through ultraviolet light and electrostatic activation. *Sci. Adv.* **2019**, *5*, eaav3430.
[187] Wu, E. X.; Xie, Y.; Liu, Q. Z.; Hu, X. D.; Liu, J.; Zhang, D. H.; Zhou, C. W. Photoinduced doping to enable tunable and high-performance anti-ambipolar $MoTe_2/MoS_2$ heterotransistors. *ACS Nano* **2019**, *13*, 5430–5438.
[188] Zhang, P. F.; Li, D.; Chen, M. Y.; Zong, Q. J.; Shen, J.; Wan, D. Y.; Zhu, J. T.; Zhang, Z. X. Floating-gate controlled programmable non-volatile black phosphorus PNP junction memory. *Nanoscale* **2018**, *10*, 3148–3152.
[189] Tian, H.; Li, L. S.; Mohammad, M. A.; Wang, X. F.; Yang, Y.; Ren, T. L. High-quality reconfigurable black phosphorus p-n junctions. *IEEE Trans. Electron Devices* **2018**, *65*, 5118–5122.
[190] Li, D.; Chen, M. Y.; Sun, Z. Z.; Yu, P.; Liu, Z.; Ajayan, P. M.; Zhang, Z. X. Two-dimensional non-volatile programmable p-n junctions. *Nat. Nanotechnol.* **2017**, *12*, 901–906.
[191] Ju, L.; Velasco, J. Jr.; Huang, E.; Kahn, S.; Nosiglia, C.; Tsai, H. Z.; Yang, W.; Taniguchi, T.; Watanabe, K.; Zhang, Y. et al. Photoinduced doping in heterostructures of graphene and boron nitride. *Nat. Nanotechnol.* **2014**, *9*, 348–352.
[192] Wang, Y.; Liu, E. F.; Gao, A. Y.; Cao, T. J.; Long, M. S.; Pan, C.; Zhang, L. L.; Zeng, J. W.; Wang, C. Y.; Hu, W. D. et al. Negative photoconductance in van der Waals heterostructure-based floating gate phototransistor. *ACS Nano* **2018**, *12*, 9513–9520.
[193] Liu, C. S.; Yan, X.; Song, X. F.; Ding, S. J.; Zhang, D. W.; Zhou, P. A semi-floating gate memory based on van der Waals heterostructures for quasi-non-volatile applications. *Nat. Nanotechnol.* **2018**, *13*, 404–410.
[194] Li, D.; Chen, M. Y.; Zong, Q. J.; Zhang, Z. X. Floating-gate manipulated graphene-black phosphorus heterojunction for nonvolatile ambipolar Schottky junction memories, memory inverter circuits, and logic rectifiers. *Nano Lett.* **2017**, *17*, 6353–6359.
[195] Vu, Q. A.; Shin, Y. S.; Kim, Y. R.; Nguyen, V. L.; Kang, W. T.; Kim, H.; Luong, D. H.; Lee, I. M.; Lee, K.; Ko, D. S. et al. Two-terminal floating-gate memory with van der Waals heterostructures for ultrahigh on/off ratio. *Nat. Commun.* **2016**, *7*, 12725.
[196] Wu, G. J.; Tian, B. B.; Liu, L.; Lv, W.; Wu, S.; Wang, X. D.; Chen, Y.; Li, J. Y.; Wang, Z.; Wu, S. et al. Programmable transition metal dichalcogenide homojunctions controlled by nonvolatile ferroelectric domains. *Nat. Electron.* **2020**, *3*, 43–50.
[197] Xiao, Z. Y.; Song, J. F.; Ferry, D. K.; Ducharme, S.; Hong, X. Ferroelectric-domain-patterning-controlled Schottky junction state in monolayer MoS_2. *Phys. Rev. Lett.* **2017**, *118*, 236801.
[198] Wang, X. D.; Wang, P.; Wang, J. L.; Hu, W. D.; Zhou, X. H.; Guo, N.; Huang, H.; Sun, S.; Shen, H.; Lin, T. et al. Ultrasensitive and broadband MoS_2 photodetector driven by ferroelectrics. *Adv. Mater.* **2015**, *27*, 6575–6581.
[199] Lee, S. J.; Lin, Z. Y.; Huang, J.; Choi, C. S.; Chen, P.; Liu, Y.; Guo, J.; Jia, C. C.; Wang, Y. L.; Wang, L. Y. et al. Programmable devices based on reversible solid-state doping of two-dimensional semiconductors with superionic silver iodide. *Nat. Electron.* **2020**, *3*, 630–637.
[200] Shi, W.; Kahn, S.; Jiang, L. L.; Wang, S. Y.; Tsai, H. Z.; Wong, D.; Taniguchi, T.; Watanabe, K.; Wang, F.; Crommie, M. F. et al. Reversible writing of high-mobility and high-carrier-density doping patterns in two-dimensional van der Waals heterostructures. *Nat. Electron.* **2020**, *3*, 99–105.
[201] Liu, Y.; Guo, J.; He, Q. Y.; Wu, H.; Cheng, H. C.; Ding, M. N.; Shakir, I.; Gambin, V.; Huang, Y.; Duan, X. F. Vertical charge transport and negative transconductance in multilayer molybdenum disulfides. *Nano Lett.* **2017**, *17*, 5495–5501.
[202] Bao, W. Z.; Cai, X. H.; Kim, D.; Sridhara, K.; Fuhrer, M. S. High mobility ambipolar MoS_2 field-effect transistors: Substrate and dielectric effects. *Appl. Phys. Lett.* **2013**, *102*, 042104.
[203] Park, H. Y.; Lim, M. H.; Jeon, J.; Yoo, G.; Kang, D. H.; Jang, S. K.; Jeon, M. H.; Lee, Y.; Cho, J. H.; Yeom, G. Y. et al. Wide-range controllable n-doping of molybdenum disulfide (MoS_2) through thermal and optical activation. *ACS Nano* **2015**, *9*, 2368–2376.
[204] Behura, S.; Berry, V. Interfacial nondegenerate doping of MoS_2 and other two-dimensional semiconductors. *ACS Nano* **2015**, *9*, 2227–2230.
[205] Utama, M. I. B.; Kleemann, H.; Zhao, W. Y.; Ong, C. S.; da Jornada, F. H.; Qiu, D. Y.; Cai, H.; Li, H.; Kou, R.; Zhao, S. H. et al. A dielectric- defined lateral heterojunction in a monolayer semiconductor. *Nat. Electron.* **2019**, *2*, 60–65.
[206] Wang, F. K.; Pei, K.; Li, Y.; Li, H. Q.; Zhai, T. Y. 2D homojunctions for electronics and optoelectronics. *Adv. Mater.* **2021**, *33*, 2005303.
[207] Liu, Y.; Duan, X. D.; Shin, H. J.; Park, S.; Huang, Y.; Duan, X. F. Promises and prospects of two-dimensional transistors. *Nature* **2021**, *591*, 43–53.
[208] Zhao, Q. H.; Jie, W. Q.; Wang, T.; Castellanos-Gomez, A.; Frisenda, R. InSe Schottky diodes based on van der Waals contacts. *Adv. Funct. Mater.* **2020**, *30*, 2001307.
[209] Wang, Y.; Kim, J. C.; Wu, R. J.; Martinez, J.; Song, X. J.; Yang, J.; Zhao, F.; Mkhoyan, A.; Jeong, H. Y.; Chhowalla, M. Van der Waals contacts between three-dimensional metals and two-dimensional semiconductors. *Nature* **2019**, *568*, 70–74.
[210] Lee, C. S.; Oh, S. J.; Heo, H.; Seo, S. Y.; Kim, J.; Kim, Y. H.; Kim, D.; Ngome Okello, O. F.; Shin, H.; Sung, J. H. et al. Epitaxial van der Waals contacts between transition-metal dichalcogenide monolayer polymorphs. *Nano Lett.* **2019**, *19*, 1814–1820.
[211] LaGasse, S. W.; Dhakras, P.; Watanabe, K.; Taniguchi, T.; Lee, J. U. Gate-tunable graphene-WSe_2 heterojunctions at the schottky-mott limit. *Adv. Mater.* **2019**, *31*, 1901392.
[212] Lv, L.; Zhuge, F. W.; Xie, F. J.; Xiong, X. J.; Zhang, Q. F.; Zhang, N.; Huang, Y.; Zhai, T. Y. Reconfigurable two-dimensional optoelectronic devices enabled by local ferroelectric polarization. *Nat. Commun.* **2019**, *10*, 3331.
[213] Agnihotri, P.; Dhakras, P.; Lee, J. U. Bipolar junction transistors in two-dimensional WSe_2 with large current and photocurrent gains. *Nano Lett.* **2016**, *16*, 4355–4360.
[214] Sze, S. M.; Ng, K. K. *Physics of Semiconductor Devices*; Wiley: Hoboken, New Jersey, 2006.
[215] Chhowalla, M.; Jena, D.; Zhang, H. Two-dimensional semiconductors for transistors. *Nat. Rev. Mater.* **2016**, *1*, 16052.
[216] Wang, Y. A.; Zheng, Y.; Han, C.; Chen, W. Surface charge transfer doping for two-dimensional semiconductor-based electronic and optoelectronic devices. *Nano Res.* **2020**, *14*, 1682–1697.
[217] Yeh, C. H.; Liang, Z. Y.; Lin, Y. C.; Chen, H. C.; Fan, T.; Ma, C. H.; Chu, Y. H.; Suenaga, K.; Chiu, P. W. Graphene-transition metal dichalcogenide heterojunctions for scalable and low-power complementary integrated circuits. *ACS Nano* **2020**, *14*, 985–992.
[218] Li, N.; Wang, Q. Q.; Shen, C.; Wei, Z.; Yu, H.; Zhao, J.; Lu, X. B.; Wang, G. L.; He, C. L.; Xie, L. et al. Large-scale flexible and transparent electronics based on monolayer molybdenum disulfide

field-effect transistors. *Nat. Electron.* **2020**, *3*, 711–717.
[219] Wang, H.; Yu, L. L.; Lee, Y. H.; Shi, Y. M.; Hsu, A.; Chin, M. L.; Li, L. J.; Dubey, M.; Kong, J.; Palacios, T. Integrated circuits based on bilayer MoS_2 transistors. *Nano Lett.* **2012**, *12*, 4674–4680.
[220] Li, Z. C.; Shu, W. N.; Li, Q. Q.; Xu, W. T.; Zhang, Z. W.; Li, J.; Wang, Y. L.; Liu, Y. Y.; Yang, J. H.; Chen, K. Q. et al. Nondegenerate P-type in-doped SnS_2 monolayer transistor. *Adv. Electron. Mater.* in press, DOI: 10.1002/aelm.202001168.
[221] Tang, J.; Wei, Z.; Wang, Q. Q.; Wang, Y.; Han, B.; Li, X. M.; Huang, B. Y.; Liao, M. Z.; Liu, J. Y.; Li, N. et al. *In situ* oxygen doping of monolayer MoS_2 for novel electronics. *Small* **2020**, *16*, 2004276.
[222] Qiu, Q. X.; Huang, Z. M. Photodetectors of 2D materials from ultraviolet to terahertz waves. *Adv. Mater.* **2021**, *33*, 2008126.
[223] Pu, J.; Takenobu, T. Monolayer transition metal dichalcogenides as light sources. *Adv. Mater.* **2018**, *30*, 1707627.
[224] Xie, C.; Mak, C.; Tao, X. M.; Yan, F. Photodetectors based on two-dimensional layered materials beyond graphene. *Adv. Funct. Mater.* **2017**, *27*, 1603886.
[225] Buscema, M.; Groenendijk, D. J.; Steele, G. A.; van der Zant, H. S. J.; Castellanos-Gomez, A. Photovoltaic effect in few-layer black phosphorus PN junctions defined by local electrostatic gating. *Nat. Commun.* **2014**, *5*, 4651.
[226] Shirasaki, Y.; Supran, G. J.; Bawendi, M. G.; Bulović, V. Emergence of colloidal quantum-dot light-emitting technologies. *Nat. Photonics* **2013**, *7*, 13–23.
[227] Lopez-Sanchez, O.; Lembke, D.; Kayci, M.; Radenovic, A.; Kis, A. Ultrasensitive photodetectors based on monolayer MoS_2. *Nat. Nanotechnol.* **2013**, *8*, 497–501.
[228] Kufer, D.; Konstantatos, G. Highly sensitive, encapsulated MoS_2 photodetector with gate controllable gain and speed. *Nano Lett.* **2015**, *15*, 7307–7313.
[229] Chen, J.; Wang, Q. Y.; Sheng, Y. C.; Cao, G. Q.; Yang, P.; Shan, Y. B.; Liao, F. Y.; Muhammad, Z.; Bao, W. Z.; Hu, L. G. et al. High-performance WSe_2 photodetector based on a laser-induced p-n junction. *ACS Appl. Mater. Interfaces* **2019**, *11*, 43330–43336.
[230] Tu, L. Q.; Cao, R. R.; Wang, X. D.; Chen, Y.; Wu, S. Q.; Wang, F.; Wang, Z.; Shen, H.; Lin, T.; Zhou, P. et al. Ultrasensitive negative capacitance phototransistors. *Nat. Commun.* **2020**, *11*, 101.